processes

MDPI

Article

Tectono-Climatic Coupling Across the Foreland-to-Rift Transition Controls Vertical Source-Rock Heterogeneity in the Triassic–Jurassic Succession of the Northern Kuqa Depression, Tarim Basin, NW China

Wanle Liang [1,2,3], Xianqing Li [2,3,*], Qiang Wei [4], Guangjie Zhao [2,3], Jin Li [5], Mancang Liu [5] and Zhongyao Xiao [6]

[1] Research Institute of Exploration and Development, Sinopec Jianghan Oilfield Company, Wuhan 430223, China
[2] State Key Laboratory for Fine Exploration and Intelligent Development of Coal Resources, China University of Mining and Technology (Beijing), Beijing 100083, China
[3] College of Geoscience and Surveying Engineering, China University of Mining and Technology (Beijing), Beijing 100083, China
[4] School of Resources and Civil Engineering, Suzhou University, Suzhou 234000, China
[5] PetroChina Research Institute of Petroleum Exploration & Development, Beijing 100083, China
[6] Research Institute of Exploration and Development, Tarim Oilfield Company, PetroChina, Korla 841000, China
* Correspondence: lixq@cumtb.edu.cn

Abstract

Vertical heterogeneity is the main obstacle to predicting effective source rocks in lacustrine superimposed basins; yet, its origin remains poorly resolved because most studies examine a single interval or a single control. Five Triassic–Jurassic source-rock units (Huangshanjie, Taliqike, Yangxia, Kezilenuer and Qiakemake formations) of the northern Kuqa Depression were therefore analyzed within one organic–inorganic framework combining Rock-Eval pyrolysis, organic petrology, molecular biomarkers, and major- and trace-element geochemistry (redox proxies, Sr/Ba paleosalinity and the chemical index of alteration, CIA). Weathering, Rock-Eval matrix, and thermal-maturity effects were screened explicitly and do not control the between-horizon contrasts. Stable Al_2O_3–TiO_2, Ti/Al, and SiO_2/Al_2O_3 relations show that provenance was constant, so the contrasts between horizons record environmental change. Across the foreland-to-rift transition marked by the Triassic–Jurassic angular unconformity, lake hydrology and hydrochemistry evolved from suboxic brackish–fresh stratified lakes, through freshwater swamps and oxic deltaic systems, to a brackish, dysoxic semi-deep lake; organic-matter (OM) sources co-evolved from aquatic, through mixed terrigenous–aquatic and higher-plant plus algal, to terrigenous and, finally, phytoplankton dominance. Source-rock quality was set not by any single factor but by the shifting balance among productivity, preservation, and clastic dilution, whose relative weighting was reset when the basin changed type: the TOC maximum (29.1 wt %) and the hydrogen-index maximum (775 mg HC/g TOC) fall in different units and record opposite environmental configurations. Because no single parameter ranks the horizons correctly, a depositional model calibrated on one interval cannot be extrapolated across a change in basin type. The resulting coupled model explains why chemically distinct intervals stack vertically and yields a transferable prediction workflow for analogous basins.

Keywords: source rock heterogeneity; organic–inorganic geochemistry; paleoenvironmental evolution; chemical index of alteration; biomarkers; superimposed basin; Kuqa Depression; Tarim Basin

Check for updates

Received: 14 August 2026
Revised: 7 October 2026
Accepted: 19 October 2026
Published: 29 October 2026

Copyright: © 2026 by the authors. Licensee MDPI, Basel, Switzerland. This article is an open access article distributed under the terms and conditions of the Creative Commons Attribution (CC BY) license.

1. Introduction

Lacustrine and coal-bearing successions host a large share of the world's continental hydrocarbon resources [1,2], and across the Tarim, Junggar, Bohai Bay, Ordos, and Songliao basins, the distribution of lacustrine source rocks governs resource endowment [3–5]. Ancient lakes are comparatively small, hydrologically closed or semi-closed systems with short water-residence times, so they respond far more sensitively than open marine systems to tectonic and climatic forcing; their organic sedimentary facies vary strongly both vertically and laterally, and the resulting source-rock heterogeneity directly affects resource potential and the selection of exploration targets [6,7], so reconstructing the paleoenvironmental processes behind it is a prerequisite for reliable prediction rather than a descriptive exercise [8,9]. The individual controls on lacustrine organic-matter (OM) enrichment are well documented [10,11]: lake-basin type fixes the ratio of accommodation to the combined supply of sediment and water and hence the broad hydrocarbon-generation potential [12]; sedimentation rate acts non-monotonically, since low rates expose OM to prolonged oxidation at the sediment–water interface, whereas high rates dilute it with clastic material [13]; and paleoclimate, tectonism, productivity, preservation, and dilution interact over short spatial and temporal scales, one force commonly acting on several of these terms at once and in opposite senses [14]. Most depositional models built on these controls, however, describe single-phase lacustrine rift basins [15].

Superimposed basins pose a distinct and largely unresolved version of the problem [16,17]. Where genetically different basin phases are stacked, a compressional foreland succeeded by an extensional rift—for example, the accommodation regime, subsidence rate, drainage configuration, and lake hydrochemistry—are all reorganized at the phase boundary [18,19]; yet, the resulting source rocks are preserved within a single, apparently continuous section that records a composite of environments governed by different tectonic boundary conditions rather than a monotonic record of progressive lake evolution. A study restricted to one interval therefore cannot in principle recover the mechanism that organizes the heterogeneity because that mechanism becomes visible only when successive phases are compared, and organic data alone cannot separate productivity, preservation, and dilution because bulk pyrolysis and biomarkers respond to their combined effect [13]; so, an independent inorganic constraint on weathering intensity, hydrochemistry, and redox state is required.

The northern tectonic belt of the Kuqa Depression, NW China (Figure 1), offers an unusually complete natural laboratory for this problem. The depression is one of the most important hydrocarbon-rich superimposed basins in western China [20,21], and its Triassic–Jurassic succession contains five thick source-rock units deposited across the foreland-to-rift transition and exposed in continuous outcrop along the piedmont, so the entire column can be sampled systematically rather than reconstructed from scattered well penetrations, and climatic and tectonic change, both of which the succession registers, can in principle be separated. Previous work on the succession has characterized hydrocarbon-generation potential and generation kinetics [22–24], documented the geochemistry, depositional environment, and development model of the Jurassic coal-measure source rocks and mapped source-rock distribution in the Tugerming area [4,25,26], reported biomarker assemblages, and reconstructed hydrocarbon charging and accumulation [27,28]; most recently, it addressed differential OM enrichment in Middle–Upper Triassic lacustrine mudstones by integrated organic–inorganic analysis [29]. These studies established the source-rock inventory of the belt, but they share three limitations that the present study is designed to overcome: quantitative inorganic constraints are largely absent, so weathering intensity, paleosalinity, and redox state remain unquantified; single intervals or sub-areas are treated in isolation rather than the full column spanning the change in basin type; and the emphasis falls

on static characterization rather than on the evolutionary mechanism that generates the vertical heterogeneity.

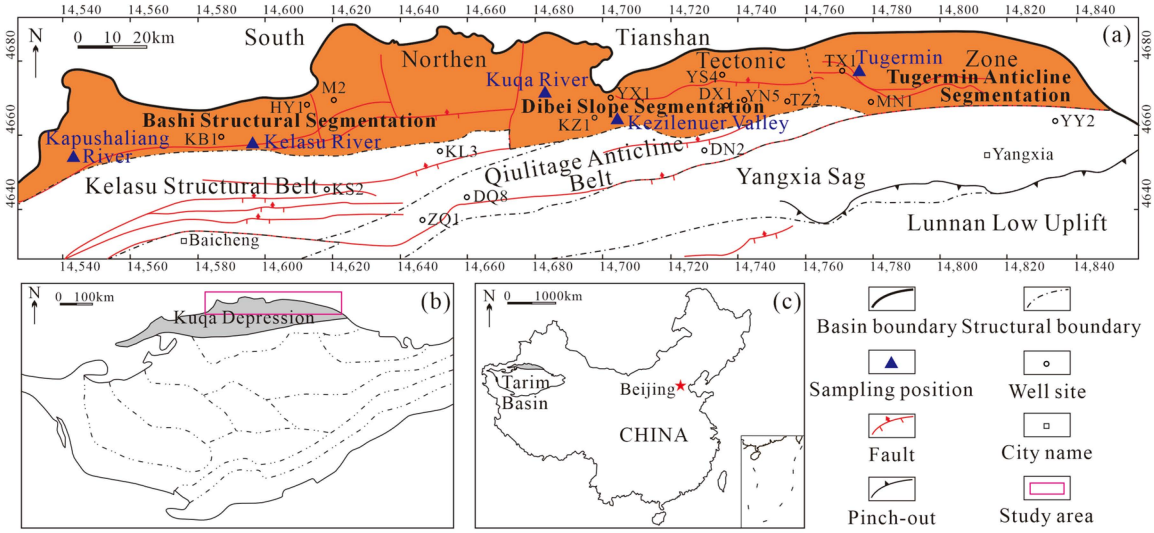


Figure 1. Geological setting of the study area. (**a**) Structural subdivision of the northern tectonic belt of the Kuqa Depression (orange-shaded area), showingthe five sampled outcrop sections (triangles) and nearby wells; (**b**) location of the Kuqa Depression within the Tarim Basin; (**c**) location of the Tarim Basin in NW China. Drawn by the authors from their own field mapping and GPS-located outcrop sections [30].

Accordingly, this study integrates organic and inorganic geochemistry (Rock-Eval bulk parameters, organic petrography, biomarker distributions, and major- and trace-element data, the last of these including redox indicators, Sr/Ba salinity indices, and the CIA) to reconstruct the coupled evolution of depositional environment and OM source across all five Triassic–Jurassic horizons and tests three hypotheses. (**H1**) If the vertical geochemical contrasts between horizons reflect environmental rather than provenance change, they should be accompanied by stable detrital-source indicators. (**H2**) If basin-type switching from a foreland to an extensional-rift regime, together with CIA-recorded paleoclimate, controlled lake hydrology and hydrochemistry, then the biotic community and primary productivity should change systematically across the phase boundary. (**H3**) If source-rock quality was determined not by any single control but by the interplay among productivity, preservation, and dilution, then no single proxy should rank the five horizons correctly, and the relative weighting of the three controls should shift from horizon to horizon. The novelty of the resulting coupled, mechanism-based model lies not in re-characterizing the source rocks but in identifying the tectono-climatic mechanism that organizes their heterogeneity in a form transferable to other lacustrine superimposed basins.

2. Geological Setting

2.1. Tectonic Framework and Basin-Phase Evolution

The Kuqa Depression is a superimposed foreland basin dominated by Meso–Cenozoic sedimentation [31,32]. It developed on a Paleozoic folded basement before the Late Permian and records three genetically distinct basin phases: a Late Permian–Triassic foreland basin, a Jurassic–Paleogene extensional-rift basin, and a Neogene–Quaternary rejuvenated foreland basin [31]. This succession of phases, the defining attribute of a superimposed basin, is central to the present study. The foreland phase was characterized by flexural subsidence in front of the rising orogen, high sediment supply from a proximal source, and comparatively rapid burial [17]; the rift phase was governed by extensional, fault-

controlled subsidence with more localized depocenters, lower average sediment flux, and generally greater accommodation relative to supply [19]. Because lake-basin type, and with it hydrocarbon-generation potential, depends on how accommodation compares with the combined sediment and water supply [12], the foreland-to-rift transition should be recorded directly by the source rocks that span it.

Critically for the present interpretation, that transition is not inferred solely from subsidence modeling: it is expressed physically in the stratigraphy as a regional angular unconformity at the base of the Lower Jurassic Ahe Formation, produced by regional uplift and erosion at the Triassic–Jurassic boundary (Figure 2). This surface separates the Triassic braided-delta to deep-lacustrine succession that hosts the Huangshanjie and Taliqike source rocks from the Jurassic deltaic to shore–shallow lacustrine succession that hosts the Yangxia, Kezilenuer, and Qiakemake source rocks, and it therefore provides an independent, mappable datum against which the geochemical record can be read. A second, more intense angular unconformity separates the Mesozoic succession from the underlying Permian.

Owing to strong uplift of the southern Tianshan, the northern tectonic belt formed comparatively early and developed imbricate thrust faults [33]. It is subdivided from west to east into the Bashi structural segment, the Dibei slope, and the Tugerming anticline segment [34] (Figure 1a). The belt occupies the piedmont zone of the depression across an exploration area of approximately 5.9×10^3 km^2, and the high-yield drilling of Well Dixi-1 in 2012 opened tight-gas exploration in the area and established it as a strategic successor region for the West-to-East Gas Pipeline project [35]. Present-day structural relief brings the Mesozoic succession to outcrop along the piedmont, which is what makes continuous sampling of the full source-rock column possible.

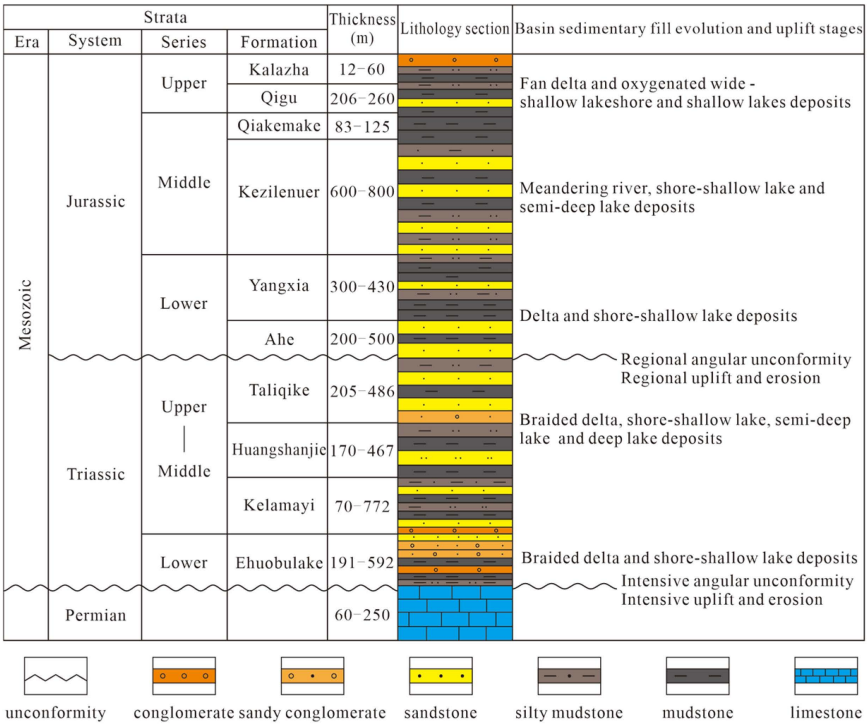


Figure 2. Generalized Permian–Jurassic stratigraphic column of the Kuqa Depression, showing formation thicknesses, lithology, the five source-rock units, and the sedimentary-fill and uplift stages. The regional angular unconformity at the base of the Ahe Formation marks the foreland-to-rift transition used in this study as the basin-phase boundary. Adapted with permission from [35]. Copyright 2020 John Wiley & Sons Ltd.

2.2. Mesozoic Depositional and Climatic Evolution

During the Mesozoic, the belt was a continental lacustrine basin with a lake–river–delta depositional system [36]. Early Triassic provenance lay in the ancient Tianshan, from which detrital material was transported into the depression [37]; braided-delta and shore-shallow-lake deposits accumulated at that time (Figure 2). Middle Triassic sediments accumulated in a progressively deepening lake under a humid climate in which freshwater plants flourished [23]. Before the middle Late Triassic, subdued tectonism and lake expansion produced the semi-deep to deep lacustrine Huangshanjie Formation; the overlying Upper Triassic Taliqike Formation formed by lakeshore-swamp deposition. Regional uplift and erosion then terminated the Triassic cycle. By the Early Jurassic, deltaic and shore-shallow-lake systems prevailed. In the late Middle Jurassic, the depositional area contracted to shore–shallow and semi-deep lakes, lacking meandering rivers and deltas. During the Late Jurassic, lake siltation and fluvial deposition dominated as the Tarim Basin was uplifted under a semi-arid climate [38]. The paleontological record is consistent with this trajectory: biotic assemblages of plants, sporopollen, conchostracans, bivalves, and acritarchs indicate freshwater conditions through much of the Late Triassic–Middle Jurassic interval, and the ecological affinities of the sporopollen parent plants record a progressive shift from tropical–subtropical, through subtropical warm–temperate, to subtropical climates [37,39].

2.3. The Source-Rock Succession

The central subsidence axis of the Mesozoic basin coincides with the present-day piedmont zone, where the source rocks are thickest and best preserved [40]. Five thick source-rock units occur in the Middle–Upper Triassic and Lower–Middle Jurassic succession, in ascending order the Huangshanjie (170–467 m), Taliqike (205–486 m), Yangxia (300–430 m), Kezilenuer (600–800 m), and Qiakemake (83–125 m) formations, with a combined present-day thickness exceeding 1000 m (Figure 2) [39]. The lower two units belong to the foreland phase and the upper three to the extensional-rift phase, so that the basin-type boundary lies between the Taliqike and Yangxia formations, at the regional angular unconformity beneath the Ahe Formation. The five units are lithologically diverse, ranging from dark mudstone and shale through carbonaceous mudstone to coal, and this diversity is itself the expression of the heterogeneity that the present study seeks to explain.

3. Materials and Methods

3.1. Samples and Sampling Strategy

Forty-six outcrop samples were collected from the five Triassic–Jurassic units across the northern tectonic belt (Figure 1a): 10 from the Kapushaliang River section, 9 from the Kelasu River section, 10 from the Kuqa River section, 10 from the Kezilenuer Valley section, and 7 from the Tugerming section. The sampling design was intended to isolate stratigraphic variation from structural and weathering artifacts. To minimize tectonic disturbance, fault zones and their damage aureoles were avoided, and samples were taken systematically from a single continuous outcrop within each section, following lithological variation rather than a fixed spacing, so that every lithofacies present in a unit is represented. To limit alteration by surface weathering, weathered surfaces were removed in the field, and approximately 2 kg of fresh rock was recovered at each site. All samples were crushed and ground to <80 mesh for total organic carbon (TOC) analysis, Rock-Eval pyrolysis, and group-component separation; splits were reserved for organic petrology, elemental analysis, and solvent extraction.

Table 1 lists the number of samples analyzed per formation, section, and technique. All 46 samples were analyzed for TOC, Rock-Eval pyrolysis, and organic petrology; a subset of 32 samples, chosen so that every formation is represented in at least three sections, was

analyzed for major and trace elements; and 18 samples covering all five formations were extracted for biomarker analysis. Each formation is therefore represented by 9–10 bulk, 6–8 elemental, and 2–7 molecular analyses. The molecular data for the Kezilenuer Formation come from a single section (Kuqa River), a limitation noted in Section 5.8.

Table 1. Distribution of the 46 outcrop samples by formation, section, and analytical technique. Entries give the number of samples analyzed for bulk organic geochemistry and organic petrology (TOC, Rock-Eval pyrolysis, maceral analysis, and R_o)/major- and trace-element geochemistry (XRF and ICP-MS)/molecular geochemistry (solvent extraction and GC–MS). Sample identifiers for each subset are listed in Tables S1–S3.

Formation	Kapushaliang River	Kelasu River	Kuqa River	Kezilenuer Valley	Tugerming	Total
Qiakemake	2/2/1	3/1/0	2/1/0	2/2/1	0/0/0	9/6/2
Kezilenuer	3/1/0	0/0/0	3/3/2	3/2/0	0/0/0	9/6/2
Yangxia	2/1/1	0/0/0	2/2/2	2/2/1	4/3/3	10/8/7
Taliqike	2/1/1	4/2/1	1/1/0	2/2/0	0/0/0	9/6/2
Huangshanjie	1/0/0	2/2/2	2/2/2	1/0/0	3/2/1	9/6/5
Total	10/5/3	9/5/3	10/9/6	10/8/2	7/5/4	46/32/18

3.2. Analytical Methods

Carbonate was first removed with dilute HCl (HCl/H_2O = 1:7, *v/v*), after which TOC was determined on a LECO CS-230 analyzer (LECO Corporation, St. Joseph, MI, USA) [8]. For pyrolysis, 100 mg aliquots of powder were run on an OGE-II instrument (RIPED, Beijing, China): the free-hydrocarbon peak (S_1) was collected during an isothermal step at 300 °C (3 min), and the cracked-hydrocarbon peak (S_2) during heating to 650 °C at 25 °C/min, with T_{max} read at the S_2 maximum; HI follows as 100 × S_2/TOC. The recognized limitations of Rock-Eval parameters in organic-rich and coaly lithologies [41] are addressed explicitly in Sections 5.1.3 and 5.8.

Forty-six polished blocks, cut perpendicular or parallel to bedding, were prepared according to ISO 7404-2 (2009) [42] for organic petrology. Maceral analysis used visual point counting on a Leica DM4500P microscope (Leica Microsystems, Wetzlar, Germany) fitted with a CRAIC microphotometer (CRAIC Technologies, San Dimas, CA, USA) under reflected white and fluorescent light, with at least 500 points counted per sample; maceral proportions are reported in volume percent on a mineral-matter-free basis. Vitrinite reflectance (R_o) was measured under oil immersion with a 50× objective following ISO 7404-5 (2009) [43] and ASTM D7708-14 (2014) [44] after calibration against an yttrium aluminum garnet standard (R_o = 1.725%).

Thirty-two samples were ground to 200 mesh for major- and trace-element analysis. Major-element oxides were determined on an Axios mAX X-ray fluorescence (XRF) spectrometer (Malvern Panalytical, Almelo, The Netherlands): 1 g of sample was ignited at 1050 °C for 2 h to determine loss on ignition, and the residue was fused with 11 g of $Li_2B_4O_7/LiBO_2/LiBr$ (33.17%/66.33%/0.5%) flux into a glass bead; analytical precision was better than 1%. Trace elements were measured on a Thermo Scientific ELEMENT XR inductively coupled plasma mass spectrometer (ICP-MS) (Thermo Fisher Scientific, Bremen, Germany): 50 mg of sample was digested with 1.5 mL of concentrated HF and 1 mL of concentrated HNO_3 in a Teflon vessel at 190 °C for 60 h; after evaporation, the residue was redissolved in HNO_3 and ultrapure water, resealed, heated at 135 °C for 12 h, and diluted to 50 mL with 2% HNO_3. Analytical precision was better than 5%. These inorganic data underpin the paleoredox, paleosalinity, and chemical-weathering reconstructions that distinguish this study from previous, organic-only work on the belt.

Eighteen powdered samples (<80 mesh) were Soxhlet-extracted for 48 h in 250 mL of dichloromethane/methanol (93:7, *v*/*v*); asphaltenes were then precipitated over 12 h in excess *n*-hexane, and the maltene fraction was separated on a silica-gel/alumina column, eluting saturated hydrocarbons with *n*-hexane, aromatic hydrocarbons with dichloromethane/*n*-hexane (2:1, *v*/*v*), and resins with dichloromethane/methanol (2:1, *v*/*v*). Saturated and aromatic fractions were analyzed by gas chromatography–mass spectrometry (GC–MS) on an Agilent HP6890N gas chromatograph (Agilent Technologies, Santa Clara, CA, USA) coupled to a 5975I mass-selective detector fitted with an HP-5MS fused-silica capillary column, with helium carrier gas at 1 mL/min and the mass spectrometer operated in electron-impact mode (70 eV) over a scan range of 50–600 Da. For the saturated fractions, the oven was programmed from 100 °C (held 5 min) to 220 °C at 4 °C/min and then to 320 °C at 2 °C/min (held 20 min); for the aromatic fractions, from 100 °C (held 5 min) to 320 °C at 3 °C/min (held 20 min). Complete datasets are provided as Supplementary Tables S1–S3.

3.3. Geochemical Proxies and Interpretive Framework

Biomarker ratios were calculated from peak areas measured on the total ion current of the *n*-alkanes and acyclic isoprenoids and on the relevant mass chromatograms: *m*/*z* 191 for the tricyclic, tetracyclic, and pentacyclic terpanes, *m*/*z* 217 for the regular steranes and diasteranes, and the aromatic total ion current for the alkyldibenzothiophenes (ADBT) and alkyldibenzofurans (ADBF) [45]. The sterane/hopane ratio (S/H) is reported as the ratio of the total C_{27}–C_{29} regular steranes to the total C_{27}–C_{35} hopanes, and the C_{27}, C_{28}, and C_{29} regular-sterane abundances as normalized percentages of their sum.

Chemical weathering intensity was quantified using the chemical index of alteration [46], computed on a molar basis from Equation (1):

$$\mathrm{CIA} = [\mathrm{Al_2O_3}/(\mathrm{Al_2O_3} + \mathrm{CaO^*} + \mathrm{Na_2O} + \mathrm{K_2O})] \times 100 \quad (1)$$

where CaO* is the CaO held in silicate phases. CaO* was obtained in two steps, following [47]: the CaO bound in apatite was first removed with the phosphorus correction, and wherever the phosphate-corrected CaO still exceeded Na_2O (in moles), indicating a residual contribution from carbonate, CaO* was set equal to Na_2O (Equation (2)):

$$\mathrm{CaO^*} = \min[\mathrm{CaO} - (10/3) \times \mathrm{P_2O_5}, \mathrm{Na_2O}] \quad (2)$$

This procedure removes diagenetic calcite and ankerite from the CaO budget without requiring the carbonate content to be known; its sensitivity is assessed in Section 5.2 and Table S4. CIA values were plotted on an A–CN–K [Al_2O_3–(CaO* + Na_2O)–K_2O] ternary diagram, which allows any departure from the ideal weathering trend; for example, through potassium metasomatism, to be recognized before the CIA is interpreted climatically. Detrital-provenance stability was monitored using the Al_2O_3–TiO_2 correlation together with the SiO_2/Al_2O_3 and Ti/Al ratios, and lacustrine water input using Ca/Al. Paleosalinity and paleoredox state were reconstructed from elemental concentration ratios, and depositional redox conditions were constrained independently from the acyclic isoprenoids. Because no single proxy is diagnostic on its own, and because several published thresholds overlap, all proxies were interpreted jointly and only concordant signals were accepted as evidence. This concordance criterion is applied throughout Section 5. The thresholds adopted, and their sources, are summarized in Table 2.

Table 2. Geochemical proxies, threshold values, and environmental interpretation adopted in this study. TT, tricyclic terpane; TeT, tetracyclic terpane; H, hopane; ADBT, alkyldibenzothiophene; ADBF, alkyldibenzofuran; OM, organic matter; CIA, chemical index of alteration.

Proxy	Class	Threshold and Interpretation	Source
V/(V + Ni)	Redox	>0.84, euxinic; 0.60–0.84, anoxic; 0.46–0.60, dysoxic	[48]
Th/U	Redox	<2, anoxic; 2–7, oxic; >7, intensely oxidizing terrestrial	[29]
Ni/Co	Redox	<5, oxic; 5–7, dysoxic; >7, suboxic to anoxic	[48]
V/Cr	Redox	<2, oxic; 2–4.25, dysoxic; >4.25, suboxic to anoxic	[49]
Pr/Ph	Redox	>3.0, oxic; 1.0–3.0, dysoxic; <1.0, anoxic during early diagenesis	[8,49]
Sr/Ba	Salinity	<0.2, freshwater; 0.2–0.5, brackish; >0.5, marine	[50,51]
Sr content	Salinity	Higher values indicate greater evaporative concentration	[51]
CIA	Paleoclimate	Lower under cool, arid climates; higher under warm, humid climates	[7]
Ca/Al	Hydrology	Index of lacustrine water input, controlled by lake hydrochemistry	[29]
Al_2O_3–TiO_2; Ti/Al; SiO_2/Al_2O_3	Provenance	Positive Al_2O_3–TiO_2 correlation and narrow ratio ranges indicate a constant detrital source	[29]
C_{19}/C_{23}TT; C_{20}/C_{23}TT; C_{24}TeT/C_{26}TT; C_{23}TT/C_{30}H	OM source	High tricyclic and tetracyclic ratios with low C_{23}TT/C_{30}H indicate terrigenous OM	[5,9]
C_{27}–C_{28}–C_{29} regular steranes	OM source	C_{29} dominance indicates land plants and freshwater microalgae; high C_{27}, aquatic input; high C_{28}, chlorophyll-*c*-bearing phytoplankton	[5]
S/H	Productivity	High values indicate eukaryotic over prokaryotic production, eutrophication and elevated photic-zone productivity	[5,45]
ADBT/ADBF	Environment type	Discriminates marine, brackish-lacustrine, sulfate-poor lacustrine and shallow-lake/deltaic/fluvial settings	[52]

4. Results

4.1. Bulk Organic–Geochemical Parameters

Source rocks from the northern tectonic belt are generally organic-rich, but OM abundance varies strongly between horizons (Table 3 and Table S1). TOC ranges from 0.79 to 29.1 wt % across the sample set, and formation averages span 2.2–11.0 wt %, the minimum in the Huangshanjie Formation and the maximum in the coal-measure units; more than 80% of the samples exceed 2.0 wt %. HI ranges from 19 to 775 mg HC/g TOC. The two parameters are not positively related: the Taliqike and Kezilenuer formations combine the highest TOC values with among the lowest HI values, whereas the Qiakemake Formation combines more modest TOC with by far the highest HI. This decoupling is the first indication that a single control cannot account for the observed heterogeneity. Extractable OM (EOM) ranges from 0.01 to 0.79 mg/g and averages 0.19 mg/g, with the Yangxia, Taliqike, and Kezilenuer formations showing the highest formation averages (0.23–0.25 mg/g). Saturated hydrocarbons and polar compounds generally exceed aromatics; saturates dominate the Qiakemake and

Huangshanjie formations, whereas polar compounds prevail in the Kezilenuer, Taliqike, and Yangxia formations.

Table 3. Formation-by-formation summary of the measured organic and inorganic geochemistry. TOC, total organic carbon; HI, hydrogen index; R_o, vitrinite reflectance; CIA, chemical index of alteration. Ranges are given for TOC and HI and formation averages for R_o, CIA, and Sr. Per-sample data are given in Tables S1 and S2; the environmental interpretation of these values follows the thresholds in Table 2 and is developed in Sections 5.2 and 5.3.

Formation (Age)	TOC (wt %)	HI (mg HC/g TOC)	R_o (%)	Kerogen Type	CIA	Sr (ppm)	Dominant Macerals
Qiakemake (Middle Jurassic)	1.10–17.2	62–775	0.85	II_1–II_2	80.1	123	Exinite-rich (generally >30%)
Kezilenuer (Middle Jurassic)	1.90–23.6	26–189	0.89	II_2–III	79.5	75	Vitrinite 46–82%, inertinite 4–38%; sapropelinite 3.0%
Yangxia (Lower Jurassic)	1.70–19.3	28–461	0.88	II_1–III	81.4	122	Lowest inertinite; exinite as in Huangshanjie
Taliqike (Upper Triassic)	2.40–29.1	19–159	1.12	II_2–III	85.5	76	Vitrinite 38–85%, inertinite 2–47%; sapropelinite 6.8%
Huangshanjie (Middle–Upper Triassic)	0.79–4.5	20–200	1.22	II_2–III	83.0	126	Highest sapropelinite; relatively low vitrinite

4.2. Maceral Composition and Vitrinite Reflectance

Vitrinite (Figure 3a,b), fusinite (Figure 3c), cutinite (Figure 3d), and sporinite (Figure 3e,f) are the principal macerals; maceral proportions are listed in Table S1. Vitrinite predominates in most samples, mainly as collinite and telinite. Collinite is light to moderate gray, homogeneous, and structureless (Figure 3a), whereas telinite preserves cell structures that are commonly filled with corpohuminite or mineral matter (Figure 3b). Inertinite comprises fusinite and semifusinite; sapropelinite comprises alginite and amorphous OM; exinite comprises cutinite, sporinite, and resinite. Fusinite shows well-preserved cell structure and very high reflectance (Figure 3c), cutinite is threadlike with serrated margins (Figure 3d), and sporinite occurs as elongate threadlike bodies (Figure 3e,f). Amorphous lamalginite intergrown with a mineral–bituminous groundmass is developed in the Kezilenuer Formation (Figure 3d); this texture is interpreted in Section 5.5.

Vitrinite and inertinite contents are high in the Kezilenuer and Taliqike formations (vitrinite 38–85%, formation means 64%, and 67%; inertinite 2–47%), whereas sapropelinite is low, averaging 3.0% and 6.8% in the two units. The Huangshanjie Formation has the highest sapropelinite and relatively low vitrinite contents; the Yangxia Formation has the lowest inertinite content, a vitrinite content similar to that of the Kezilenuer and Taliqike formations, and an exinite content similar to that of the Huangshanjie Formation; and the Qiakemake Formation is characterized by abundant exinite, generally exceeding 30%. Measured R_o values range from 0.56% to 1.64%, with the highest formation average in the Huangshanjie Formation (1.22%) and the lowest in the Qiakemake and Yangxia formations (0.85% and 0.88%, respectively); the Triassic units are therefore slightly more mature than the Jurassic ones, consistent with their greater burial depth.

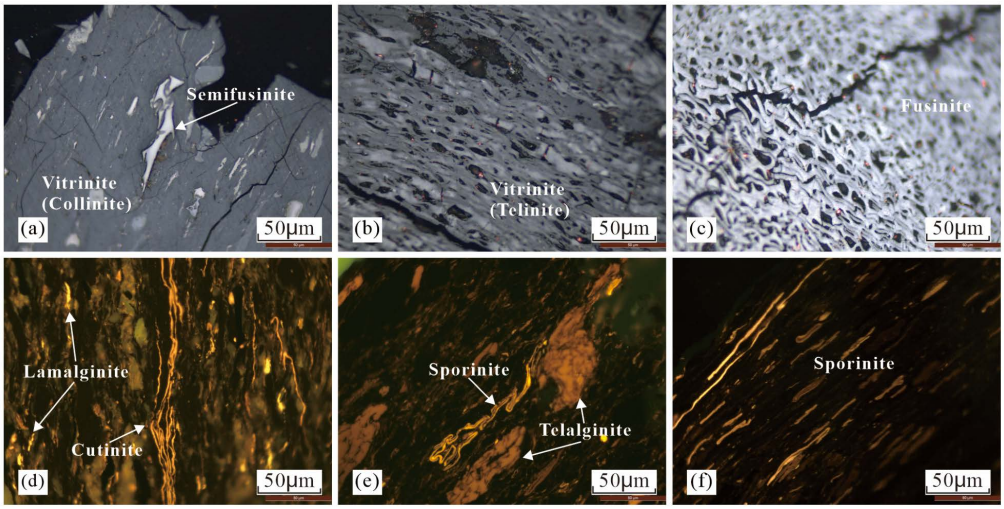


Figure 3. Photomicrographs of macerals in source rocks from the northern tectonic belt. (**a**) Collinitic vitrinite with semifusinite, sample KPL1, Huangshanjie Fm., reflected white light; (**b**) telinitic vitrinite, KCH3, Taliqike Fm., reflected white light; (**c**) fusinite with well-preserved cell structure, KZL2, Taliqike Fm., reflected white light; (**d**) lamalginite and cutinite, KCH8, Kezilenuer Fm., fluorescence; (**e**) sporinite and telalginite, TGE4, Yangxia Fm., fluorescence; (**f**) sporinite, KCH1, Huangshanjie Fm., fluorescence.

4.3. Major- and Trace-Element Composition

Major-element contents vary widely (Table 3 and Table S2). SiO_2 ranges from 10.5% to 64.9%, with higher formation averages in the Huangshanjie (51.5%), Qiakemake (48.1%), and Yangxia (47.9%) formations than in the Taliqike (41.9%) and Kezilenuer (31.4%) formations; the low silica contents of the latter two units reflect their high organic and clay contents rather than a change in detrital composition. CaO, Na_2O, and Al_2O_3 are relatively enriched in the Huangshanjie and Qiakemake formations. SiO_2/Al_2O_3 ranges from 1.81 to 8.94, Al_2O_3 and TiO_2 are positively correlated ($r^2 = 0.66$), and Ti/Al ranges only from 0.03 to 0.11. Trace elements show systematic contrasts: Ba, Sr, and V have high average contents (584, 106, and 100 ppm, respectively), whereas Co, Th, and U average 13.2, 12.2, and 3.6 ppm. CIA values fluctuate only slightly, being highest in the Taliqike Formation (average 85.5) and lowest in the Kezilenuer and Qiakemake formations (79.5 and 80.1); the Huangshanjie and Yangxia formations are intermediate. Formation averages are summarized in Table 3 and are interpreted in Sections 5.2 and 5.3.

4.4. Molecular Biomarker Characteristics

Normalized C_{12}–C_{38} *n*-alkane distributions show that low-molecular-weight compounds dominate the extracts (Figure 4). The carbon preference index (CPI) ranges from 1.09 to 1.57 and the odd–even predominance (OEP) from 0.93 to 1.37, both with the highest averages in the Kezilenuer and Taliqike formations; CPI is lowest in the Qiakemake Formation (average 1.11) and OEP lowest in the Huangshanjie and Qiakemake formations (averages 1.11 and 1.08). Overall averages are 1.26 for CPI and 1.12 for OEP.

Pristane/phytane (Pr/Ph) ranges from 0.61 to 8.8, and Pr/nC_{17} and Ph/nC_{18} from 0.16 to 3.55 and 0.09 to 2.10, respectively. The relative abundances of the C_{19}, C_{20}, and C_{23} tricyclic terpanes, the C_{24} tetracyclic terpane, gammacerane, C_{29} norhopane, C_{30} hopane, the C_{27}–C_{29} regular steranes, and the diasteranes vary considerably (Table S3; Figure 4). The Qiakemake and Huangshanjie formations show similar terpane distributions, whereas the Yangxia and Kezilenuer formations show stronger hopanes than tricyclic terpanes. Gammacerane is present in all horizons, but is generally subordinate: gammacerane/C_{30} hopane ranges from 0.02 to 0.6 and is below 0.2 in most samples, except in two Qiakemake

samples. C_{30} diahopane and the C_{27} diasteranes are conspicuous in the Qiakemake sample (Figure 4a), consistent with a clay-rich, non-euxinic depositional medium. C_{29} regular steranes are generally the most abundant, C_{28} the least abundant, and C_{27} intermediate, and for most samples, C_{28}/C_{29} is lower than C_{27}/C_{29}. Among the aromatic compounds, phenanthrene and its alkylated homologues predominate, followed by chrysene and its alkylated homologues; dibenzothiophene and dibenzofuran are present in all samples but in variable relative proportions (Figure 4).

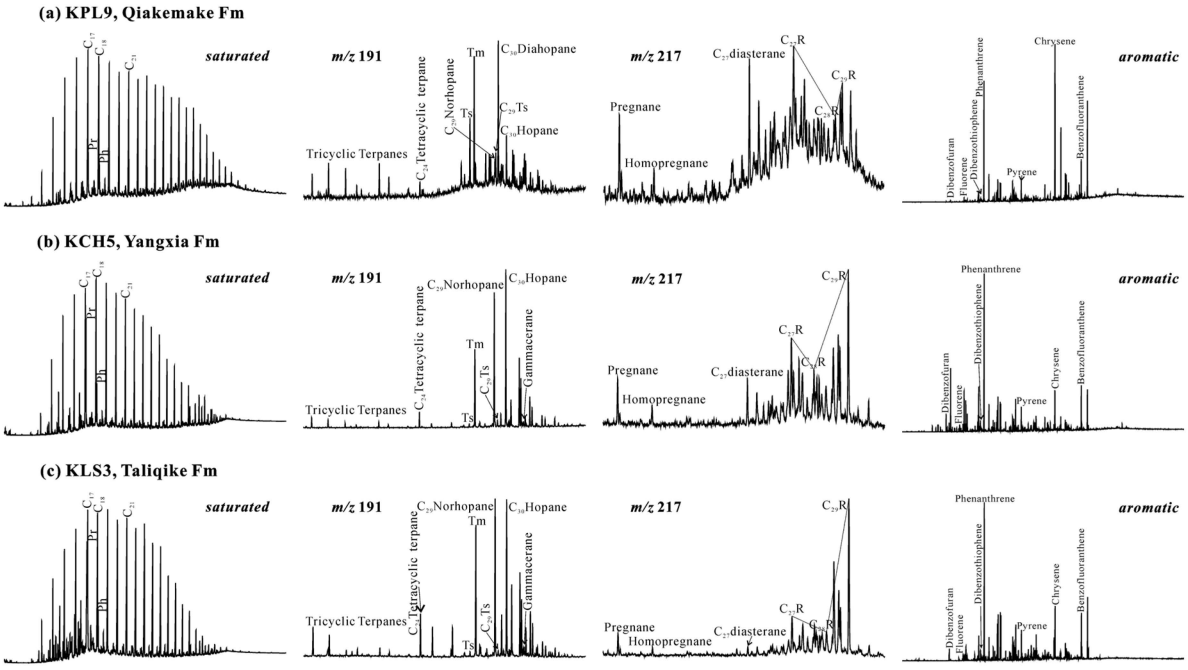


Figure 4. Representative chromatograms for samples from different horizons: gas chromatograms of the saturated fractions, *m*/*z* 191 (terpane) and *m*/*z* 217 (sterane) mass chromatograms, and total-ion chromatograms of the aromatic fractions. (**a**) KPL9, Qiakemake Fm.; (**b**) KCH5, Yangxia Fm.; (**c**) KLS3, Taliqike Fm. Pr, pristane; Ph, phytane; Ts, 18α-22,29,30-trisnorneohopane; Tm, 17α(H)-22,29,30-trisnorhopane; C_{27}R–C_{29}R, C_{27}–C_{29} regular steranes.

4.5. Summary of Vertical Variation

Taken together, the results define a column in which every measured property (OM abundance, OM type, maceral assemblage, major- and trace-element composition, and biomarker distribution) changes systematically between the five horizons, but not in a single monotonic direction. TOC and HI vary inversely between the coal-measure units and the lacustrine units; sapropelinite is highest at the base of the column and exinite at its top, while vitrinite and inertinite peak in the middle; CIA reaches a maximum in the Taliqike Formation and declines upward; Sr and Sr/Ba are highest in the units with the lowest terrigenous maceral content; and Pr/Ph differs by nearly a factor of five between the Kezilenuer and Qiakemake formations. This pattern, internally consistent within each horizon but discontinuous between them, is the observation that Section 5 sets out to explain.

5. Discussion

The discussion is organized around the three hypotheses stated in Section 1. Section 5.1 defines the heterogeneity that requires explanation and establishes the reliability of the outcrop record with respect to weathering, Rock-Eval matrix effects, and thermal maturity. Section 5.2 tests H1 by establishing provenance stability and extracting the paleoclimate signal. Sections 5.3 and 5.4 develop the environmental and OM-source records that H2

predicts. Section 5.5 assembles these into a coupled, horizon-by-horizon model, Section 5.6 tests H3, and Sections 5.7 and 5.8 set out the predictive implications and the limitations of the approach.

5.1. The Vertical Heterogeneity to Be Explained and the Reliability of the Outcrop Record

5.1.1. The Heterogeneity to Be Explained

The five horizons define a strongly heterogeneous vertical column rather than a single source-rock population. On the HI–T_{max} diagram (Figure 5), most samples fall in the type III and type II fields: the Qiakemake Formation contains type I–II kerogens, the Kezilenuer Formation mainly type II_2–III, the Yangxia Formation type II_1–III, and the Triassic samples type II_2–III, consistent with the maceral ternary plot (Figure 6a). Previous organic–geochemical studies of the belt documented these bulk characteristics and treated them as the endpoint of the analysis [4,25,26]; here they are treated instead as the signal to be explained, and the aim is to test whether that signal is organized by a common tectono-climatic mechanism.

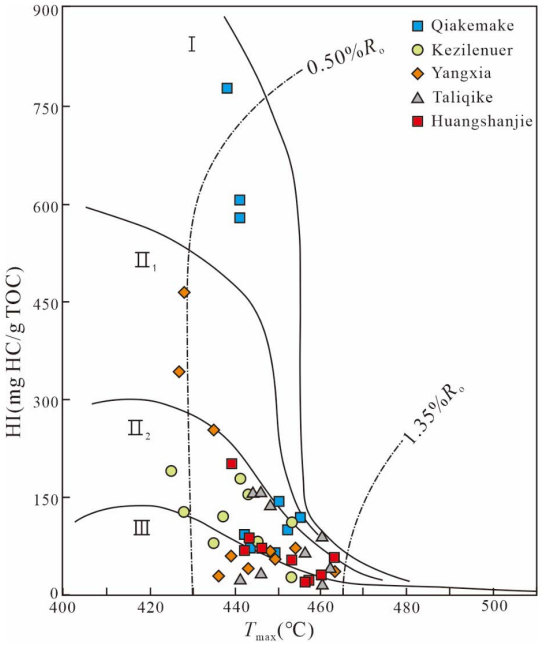


Figure 5. HI versus T_{max} for source rocks from the northern tectonic belt, showing kerogen type and thermal-maturity stage. Kerogen-type fields follow the classification of [41].

The predominance of vitrinite and inertinite indicates type III kerogen with gas-generation potential (Figure 6b): except for some Qiakemake samples, the plot data are within the carbon-enrichment field, indicating favorable gas-source characteristics. In terms of generation potential, Qiakemake samples plot in the oil and mixed-liquid-hydrocarbon field, Yangxia and Huangshanjie samples in the mixed-liquid-hydrocarbon and gas field, and Kezilenuer and Taliqike samples in the gas field. The vertical succession is therefore not only geochemically but also economically heterogeneous: liquid-prone and gas-prone intervals alternate within a single column little more than 1000 m thick, which is precisely why a mechanism-based prediction of quality, rather than a bulk average, is required.

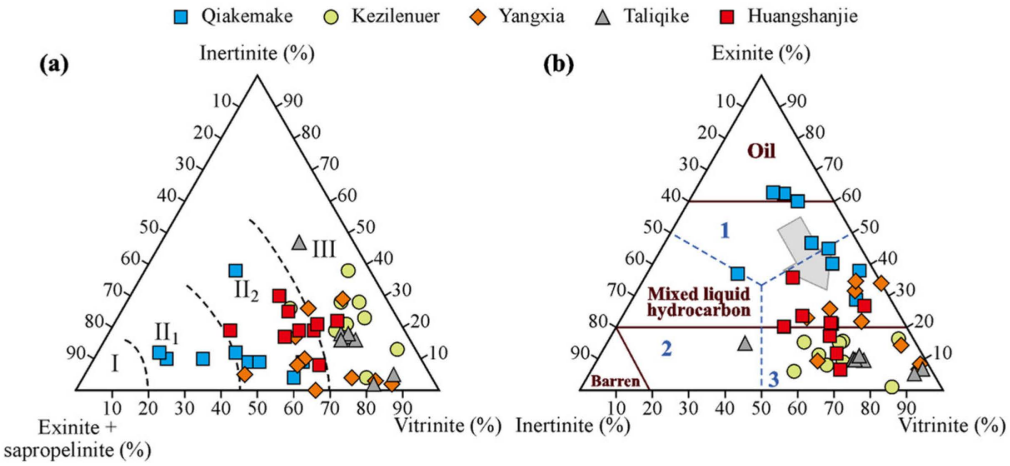


Figure 6. Maceral ternary diagrams for source rocks from the northern tectonic belt (data from Table S1). (**a**) Vitrinite–inertinite–(exinite + sapropelinite), illustrating kerogen type [53]; (**b**) inertinite–vitrinite–exinite (recalculated to 100%), showing source-rock potential (brown lines and labels [53]) together with the immature-source (1), inertinization (2) and carbon-enrichment (3) sectors (blue dashed lines) and the trend of organic maturity (grey arrow) [54].

5.1.2. Weathering Effects on Rock-Eval, Trace-Element, and Biomarker Parameters

Because all samples are from outcrop, surface weathering must be excluded as the cause of the between-horizon contrasts. Weathering lowers TOC, S_1, S_2, and HI by kerogen oxidation and loss of free hydrocarbons, removes U preferentially to Th (raising Th/U), and degrades *n*-alkanes and acyclic isoprenoids before the more resistant steranes and hopanes [55–58]. None of these signatures are systematic in the dataset (Table S5). T_{max} and R_o, two independent maturity measures, are tightly correlated ($r = 0.90$, $n = 46$) without oxidation outliers; S_1/TOC is similar in all formations (means 7.7–10.9 mg HC/g TOC); and ten of the eleven samples with TOC > 10 wt % retain HI of 120–604 mg HC/g TOC. The exception, KPL2 (Taliqike Formation; TOC 26.3 wt %, S_1 0.02 mg/g, HI 34 mg HC/g TOC), is probably partly oxidized: excluding it changes the Taliqike HI average only from 81 to 87 mg HC/g TOC and alters no ranking, but its isoprenoid ratios (Pr/Ph 0.61, Ph/nC_{18} 2.10) depart toward the biodegradation trend, so its molecular redox ratios are not used in Section 5.3. Th/U (1.4–4.8, mean 3.4) remains well below the value of 7, associated with intensely oxidizing conditions and U loss (Table 2); the eleven samples with TOC > 10 wt %, in which authigenic U would have been most vulnerable, have, if anything, lower Th/U (mean 3.1) than the others (3.5); and three of the four lowest Th/U values occur in organic-rich Kezilenuer samples; because U loss can only raise Th/U, any undetected loss would make the redox reading of Section 5.3 conservative. Within each formation, Sr/Ba is not significantly correlated with CaO ($p \geq 0.09$), so the between-formation salinity contrasts do not reflect differential carbonate dissolution, although a weak correlation across the whole dataset ($r = 0.50$) indicates a minor carbonate-hosted Sr component (Section 5.8); finally, the *n*-alkane distributions show neither an unresolved complex mixture nor loss of the short-chain homologues (<nC_{20} fraction 19–72%; Table S3).

The outcrop data also agree with published core data for the same units: Jurassic coal-measure source rocks from wells in the northern tectonic belt have HI of 50–500 mg HC/g TOC, R_o of 0.4–1.3%, Pr/Ph of 0.8–4, and mainly type II_2–III kerogen [26], ranges that encompass most of the Yangxia and Kezilenuer outcrop values (HI 26–461 mg HC/g TOC, R_o 0.56–1.36%, Pr/Ph 0.67–6.1). The between-formation differences are therefore not weathering artifacts, although absolute values from individual samples should still be treated with caution (Section 5.8).

5.1.3. Matrix Effects and Kerogen Type in the Reading of HI

HI is used here as an indicator of kerogen type, but two matrix effects limit its reliability. In organic-lean, clay-rich mudstones, the mineral matrix retains part of the pyrolysate so that S_2 and HI are underestimated, most strongly below about 2 wt % TOC [59,60]; in coals and carbonaceous mudstones, the organic matrix itself retains pyrolysate, so that vitrinite-rich humic OM commonly yields HI of only ~100–300 mg HC/g TOC even where liptinite is present, and the HI–T_{max} diagram tends to classify such samples as type III [61]. Both effects are visible here. The eight samples with TOC < 2 wt % have a mean HI of only 53 mg HC/g TOC despite a mean liptinite (exinite + sapropelinite) content of 36%, and HI is uncorrelated with liptinite across the whole dataset ($r = 0.10$, $n = 46$) but tends to increase with it; among the 16 samples with TOC > 5 wt % ($r = 0.49$, $p = 0.053$), the two highest HI values (604 and 775 mg HC/g TOC) occurred in exinite-rich Qiakemake samples. Kerogen type is therefore assigned primarily from the maceral point counts (Figure 6a; Table S1), and the HI–T_{max} plot (Figure 5) is used as a cross-check. For the coaly Taliqike and Kezilenuer intervals, which are dominated by vitrinite and inertinite, the low HI (19–189 mg HC/g TOC) is read as a record of humic OM rather than as a quantitative measure of generative potential [41]; where HI and the maceral assemblage disagree, the maceral evidence is preferred.

5.1.4. Thermal Maturity and the Independence of the Biomarker Signals

Thermal maturity must also be excluded. R_o averages 0.85–1.22% by formation (range 0.56–1.64%; Table 3), the Triassic units being slightly more mature, and CPI (average 1.26) and OEP (average 1.12) indicate a mature stage. As a molecular maturity scale, the C_{29} sterane 20S/(20S + 20R) ratio of the 18 extracts (0.20–0.45; Tables S3 and S6) increases with R_o (Spearman $\rho = 0.83$, $p < 0.001$) up to a plateau of 0.41–0.45 above $R_o \approx 0.9\%$; this plateau and the C_{29} ββ/(ββ + αα) values (0.20–0.53, uncorrelated with R_o) lie below the usual endpoints (~0.52–0.55 and ~0.67–0.71), as is common in terrigenous, coal-bearing extracts in which these ratios also depend on source and lithology [62]. Three observations show that the environmental ratios are not maturity-driven. First, the formations span overlapping R_o ranges (Table S6); yet, the ratios cluster by formation: the two Kezilenuer samples (R_o 0.61 and 0.89%) give Pr/Ph of 6.1 and 4.0, whereas the two Qiakemake samples of similar maturity (0.64 and 0.81%) both give 1.1. Second, none of the eleven source and redox ratios used in Sections 5.3 and 5.4 is correlated with R_o by Pearson correlation ($|r| \leq 0.40$, $p \geq 0.10$, $n = 18$; Table S7); T_{max} is not used as the maturity variable because, at a given R_o, it also varies with OM type [60]. Third, the two significant rank correlations do not follow maturity trends: Pr/Ph decreases with R_o ($\rho = -0.58$), opposite to the increase produced by maturation in the oil window [62], and the three highest S/H values (0.74, 0.68 and 0.52) occur at R_o of 1.36, 0.81, and 0.91%. These rank correlations reflect the co-variation of burial depth and depositional setting in the sampled sections, and the between-horizon biomarker differences can be interpreted as primarily environmental (see Section 5.8).

5.2. Provenance Stability, Chemical Weathering, and Paleoclimate

Hypothesis H1 requires that the horizon-to-horizon contrasts be environmental in origin rather than an artifact of changing detrital supply. Three independent lines of evidence support this. The positive Al_2O_3–TiO_2 correlation ($r^2 = 0.66$; Figure 7a) implies a common detrital source since both elements reside overwhelmingly in the resistant, immobile detrital fraction. The narrow Ti/Al range (0.03–0.11) and the restricted SiO_2/Al_2O_3 range (1.81–8.94) indicate that the composition of the terrigenous supply remained essentially constant throughout deposition, consistent with a single, persistent source area in the ancient Tianshan [37]. The Ca/Al ratio, which indexes lacustrine water input controlled by

lake hydrochemistry rather than by provenance, is by contrast highest in the Huangshanjie Formation (mean 0.11), lowest in the Taliqike Formation (0.02), and highly variable within the Yangxia Formation (0.03–0.19), pointing to an unstable and repeatedly renewed water body during Yangxia deposition. Provenance was therefore stable while hydrology was not, which is the pattern H1 predicts, and H1 is accordingly supported.

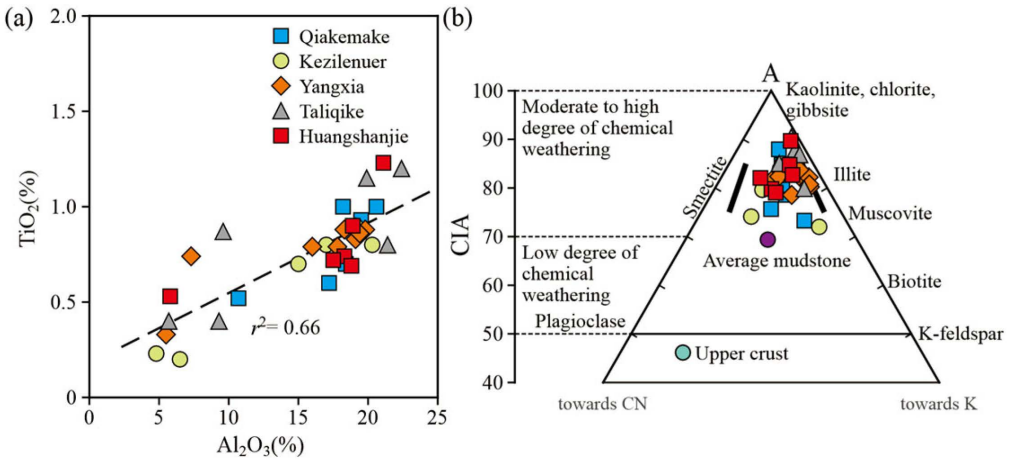


Figure 7. Provenance and chemical-weathering indicators for source rocks from the northern tectonic belt. (**a**) TiO_2 versus Al_2O_3; the positive correlation ($r^2 = 0.66$, $n = 32$) indicates a common detrital source throughout the succession. (**b**) Upper part (CIA ≥ 40) of the A–CN–K diagram [Al_2O_3 − (CaO* + Na_2O) − K_2O, molar; CaO* from Equation (2)] with the corresponding CIA scale [46]; symbols as in (**a**). The samples plot along the ideal weathering trend at moderate to high CIA, indicating a relatively warm, humid climate; average mudstone and upper continental crust are shown for reference.

With provenance held constant, the CIA becomes interpretable as a paleoclimate proxy, and it is this inorganic constraint, absent from earlier organic-only studies of the belt, that supplies the independent climatic axis on which the rest of the interpretation depends. CIA is lower for sediments deposited under cool, arid climates and higher under warm, humid climates. The formation averages listed in Table 3 peak in the Taliqike Formation (85.5) and fall to their lowest values in the Kezilenuer and Qiakemake formations (79.5 and 80.1), with the Huangshanjie and Yangxia formations in between (83.0 and 81.4); the succession therefore records a relatively warm, humid climate that peaked in the Late Triassic and waned into the Middle Jurassic. On the A–CN–K diagram (Figure 7b) all samples plot above the average-mudstone composition, indicating a moderate to high degree of chemical weathering along a trend that parallels the ideal weathering vector rather than deflecting toward the K apex; potassium metasomatism and diagenetic illitization of smectite, both of which would displace samples toward the K apex and lower their apparent CIA [63], are therefore not significant. Diagenetic carbonate is also a minor influence: CaO is low (0.1–1.5 wt %, median 0.5 wt %; Table S2), the Na_2O criterion of Equation (2) removes carbonate CaO in excess of Na_2O (operative in 18 of the 32 samples), and siderite contains neither Ca nor Na. In the sensitivity test of Table S4, omitting the CaO correction lowers the formation averages by 0.7–5.7 units, and, assuming all CaO to be carbonate-bound (CaO* = 0), raises them by 1.2–3.2 units; in every case, the Taliqike Formation has the highest average and the Taliqike–Kezilenuer contrast (4.0–7.5 units) persists, whereas the relative order of the other four formations, whose averages lie within ~3 units of one another, depends on the correction. The CIA values can therefore be read climatically, although a phase-specific correction would require XRD data (Section 5.8). The resulting CIA curve is the pivot that links basin evolution to OM accumulation in the sections that follow because

it constrains the hydrological term (precipitation and runoff) that governs both freshwater input and nutrient delivery.

5.3. Paleoredox and Paleosalinity Evolution

Paleosalinity and redox state are first-order controls on source-rock deposition, and trace-element ratios provide quantitative constraints on both [48]. Against the thresholds of Table 2, the trace-element ratios do not agree in absolute terms: V/(V + Ni) (0.64–0.85) falls mostly in the anoxic range, whereas Ni/Co (1.8–6.8) and V/Cr (0.8–2.2) fall mostly in the oxic range (Figure 8). Read jointly, as the concordance criterion of Section 3.3 requires, they indicate oxic to suboxic conditions throughout, with the least oxidizing conditions in the Taliqike Formation, which has the highest V/(V + Ni) and Ni/Co (means 0.79 and 4.7). They are less suited to ranking the other formations because Th/U and V/Cr are partly controlled by the detrital fraction: Th/U correlates with Al_2O_3 ($r = 0.59$, $n = 32$), and the organic-rich Kezilenuer samples, with the lowest Th and Cr contents of the succession (means 8.3 and 60 ppm), have low Th/U and high V/Cr, largely because these detrital elements are diluted by OM. The between-formation redox ranking is therefore taken from the isoprenoids and macerals discussed below. The absence of any euxinic signature, together with the generally low gammacerane/C_{30} hopane ratios and the prominence of C_{30} diahopane and diasteranes in the Qiakemake sample (Figure 4a), indicates that permanent, salinity-driven stratification of the kind that characterizes many saline lacustrine source-rock systems was never established in this belt [45,64]. Preservation therefore had to be achieved by other means, a point developed in Section 5.6.

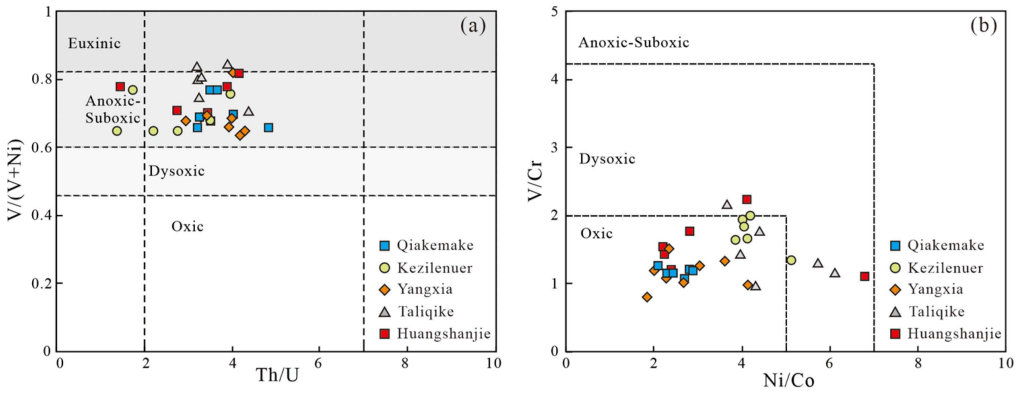


Figure 8. Cross-plots of (**a**) V/(V + Ni) versus Th/U and (**b**) V/Cr versus Ni/Co for source rocks from the northern tectonic belt. Read jointly, the ratios indicate oxic to suboxic conditions throughout (Section 5.3).

The organic–petrographic record is concordant. Inertinite has the highest reflectance among the macerals and forms preferentially in relatively open, oxidizing settings [65]; its abundance in the Kezilenuer Formation independently indicates partial oxidation of the OM before final burial. The inertinite–vitrinite–exinite plot (Figure 6b) likewise places the samples in terrigenous to marshy settings [54] in which tissue preservation and carbon enrichment were favored even where the water column itself was not reducing.

The acyclic isoprenoids provide an independent test. Pr/Ph is highest in the Kezilenuer Formation (average 5.03) and lowest in the Qiakemake Formation (average 1.08); the Huangshanjie and Yangxia formations show intermediate ratios (medians 1.4 and 2.4) that record repeated dysoxic–oxic fluctuations rather than a single stable state (Figure 9a), and the Pr/Ph of 4.2 of the only usable Taliqike extract (KLS3; Section 5.1.2) mainly reflects its terrigenous OM. The highest Pr/Ph thus occurs in the freshwater Kezilenuer Formation and the lowest in the brackish Qiakemake Formation (see below), suggesting that oxygenation was

driven by hydrological renewal rather than by shallowing alone, although in coal-bearing units, high Pr/Ph also partly reflects terrigenous OM [62]. On the Pr/nC_{17}–Ph/nC_{18} plot (Figure 9b), Kezilenuer samples fall in the oxic field with terrigenous OM, most Yangxia samples in the oxic–transitional field, and Huangshanjie and Qiakemake samples in the transitional–suboxic field with mixed or mainly algal OM; of the two Taliqike samples, KLS3 plots with the terrigenous samples and KPL2 along the biodegradation trend. The trace-element and isoprenoid records therefore agree on an oxic-to-suboxic, non-euxinic setting; within that range, the isoprenoid and maceral evidence, which is independent of detrital dilution, ranks the Kezilenuer Formation as the most oxidizing and the Qiakemake Formation as dysoxic, and the trace elements identify the Taliqike Formation as the least oxidizing.

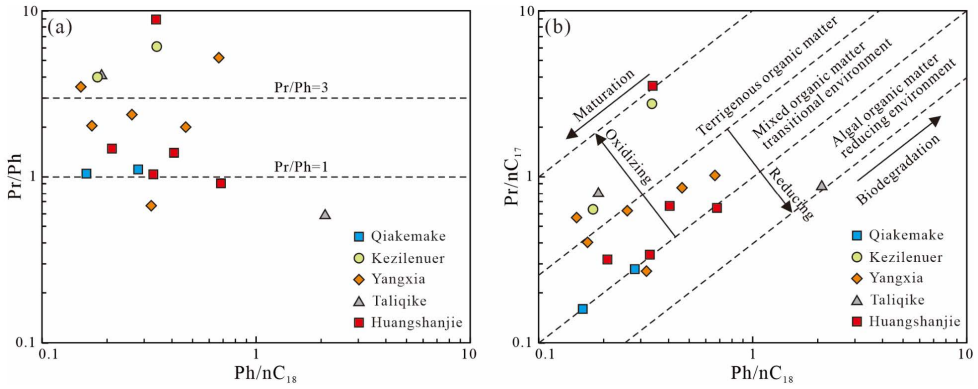


Figure 9. (**a**) Pr/Ph versus Ph/nC_{18} and (**b**) Pr/nC_{17} versus Ph/nC_{18} for source rocks from the northern tectonic belt, showing redox conditions, OM source, and thermal maturity.

Paleosalinity, reconstructed from Sr contents and Sr/Ba ratios, records the hydrological counterpart of these changes. With the thresholds of Table 2, the Huangshanjie and Qiakemake formations (Sr/Ba means 0.31 and 0.28; Sr 126 and 123 ppm) were deposited in brackish water, the Yangxia Formation mainly in fresh water with brackish excursions (median 0.16, range 0.11–0.75), and the Taliqike and Kezilenuer formations (means 0.18 and 0.11; Sr 76 and 75 ppm) in fresh water. Salinity was thus lowest in the two coal-bearing units and highest in the two units with the most aquatic OM. Because humid climates and open, through-flowing drainage both freshen a lake, whereas evaporation and hydrological restriction raise its salinity [50,51], salinity tracks climate and hydrological openness jointly rather than CIA alone: the freshwater Taliqike Formation coincides with the CIA maximum; the equally fresh Kezilenuer Formation, despite the lowest CIA, records an open, inflow-dominated delta-front setting (Section 5.5); and salinity rose again only when the lake became restricted during Qiakemake deposition. This coupling of the weathering and salinity signals to lake hydrology provides the first direct quantitative support for H2.

5.4. Organic-Matter Input and Primary Producers

On the maceral ternary plot (Figure 6a), Qiakemake samples fall in the type II_1–II_2 fields, indicating a mixed source of algae, other aquatic organisms, and higher plants; Yangxia and Huangshanjie samples contain type II_2–III kerogens, indicating a significant terrigenous contribution; and Kezilenuer and Taliqike samples contain type III kerogens, indicating terrigenous dominance. Sapropelinite comprises telalginite, derived from solitary and colonial algae, and lamalginite, derived from planktonic and benthic organisms [11]; its relatively high abundance in the Huangshanjie Formation records a substantial aquatic OM input, whereas the very high combined vitrinite, inertinite, and exinite contents of

the Kezilenuer and Taliqike formations signal the greatest terrigenous input of the succession [65].

Terpane parameters constrain the terrigenous contribution independently of the macerals [9]. C_{24}TeT/C_{26}TT is strongly correlated with C_{19}/C_{23}TT ($r^2 = 0.59$, $n = 18$, $p < 0.001$) but only weakly with Pr/Ph ($r^2 = 0.16$; Figure 10), and high C_{19}/C_{23}TT, C_{20}/C_{23}TT, and C_{24}TeT/C_{26}TT indicate terrigenous OM [5]. The Yangxia and Taliqike formations have the highest C_{24}TeT/C_{26}TT (means 7.71 and 7.18), followed by the Huangshanjie (4.64), Kezilenuer (3.46), and Qiakemake (1.23) formations; C_{19}/C_{23}TT and C_{20}/C_{23}TT are likewise high in the Taliqike, Huangshanjie, and Yangxia formations (means 2.43–2.69 and 1.78–2.10), intermediate in the Kezilenuer Formation (1.48 and 1.27), and lowest in the Qiakemake Formation (0.56 and 0.86). The terpanes and the macerals therefore agree in identifying the Qiakemake Formation as the least terrigenous unit and the Taliqike and Yangxia formations as strongly terrigenous; the Kezilenuer Formation, terrigenous by maceral composition, has only intermediate tricyclic ratios, which rest on two samples from a single section.

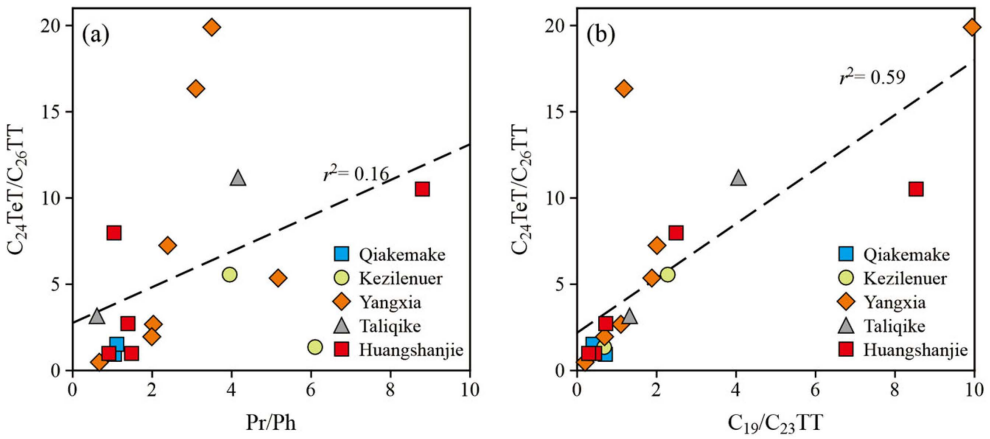


Figure 10. Cross-plots of C_{24}TeT/C_{26}TT versus (**a**) Pr/Ph and (**b**) C_{19}/C_{23}TT for source rocks from the northern tectonic belt (data from Table S3). The correlation in (**b**) ($r^2 = 0.59$, $n = 18$, $p < 0.001$) shows that both ratios are carried by the same terrigenous flux; the correlation in (**a**) is weak ($r^2 = 0.16$, $p = 0.10$).

The regular-sterane order ($C_{29} > C_{27} > C_{28}$) indicates a greater land-plant than aquatic contribution overall, although the high C_{27} contents imply a variable aquatic input (Figure 11). C_{29}-sterane abundance increases with C_{24}TeT/C_{26}TT ($r = 0.51$, $p = 0.03$) and, less clearly, with C_{19}/C_{23}TT ($r = 0.38$, $p = 0.12$) (Figure 12a,b), consistent with the view that the C_{29} signal is carried by the same terrigenous flux that the terpanes record. The Huangshanjie and Yangxia formations have similar C_{27}/C_{29} ratios, but the Yangxia Formation has a markedly higher C_{24}TeT/C_{26}TT (7.71 versus 4.64) and therefore received more higher-plant material, whereas the Huangshanjie Formation received more algae. The Kezilenuer Formation has the highest C_{29}-sterane abundance, consistent with a combined higher-plant and freshwater-microalgal source, and the Taliqike Formation has a slightly higher C_{28}-sterane abundance (mean 20.5%, $n = 2$) than the other units, which may indicate a minor contribution from chlorophyll-*c*-bearing phytoplankton.

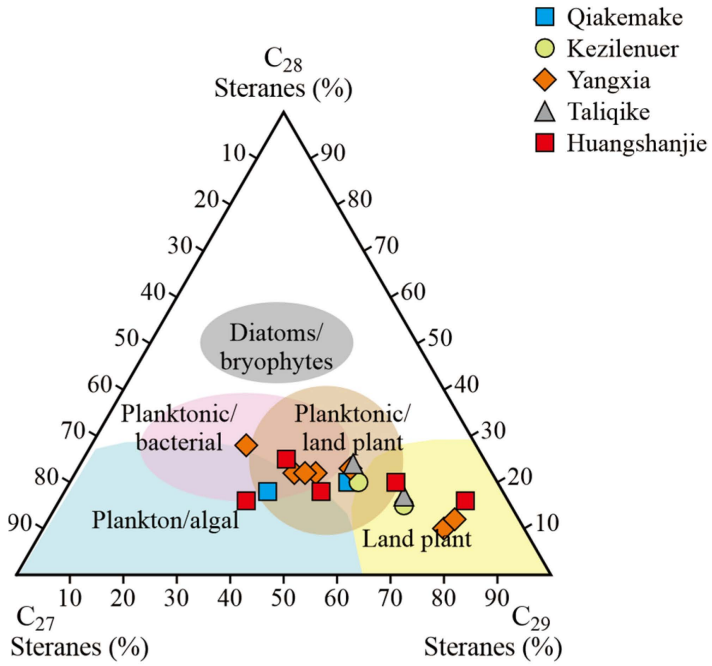


Figure 11. Ternary diagram of the C_{27}, C_{28}, and C_{29} regular steranes for source rocks from the northern tectonic belt, showing the organic-matter source (data for the 18 extracted samples from Table S3; source fields modified after [66]).

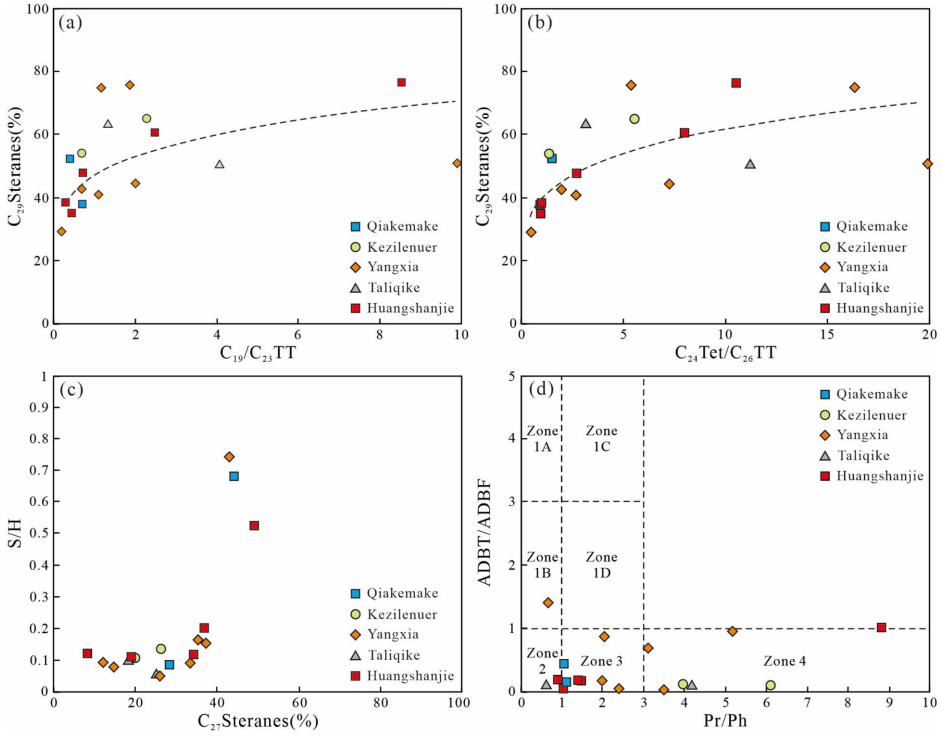


Figure 12. Relative abundances of selected saturated and aromatic biomarkers for source rocks from the northern tectonic belt. (**a**) C_{29} steranes versus $C_{19}/C_{23}TT$; (**b**) C_{29} steranes versus $C_{24}TeT/C_{26}TT$; (**c**) S/H versus C_{27} steranes; (**d**) ADBT/ADBF versus Pr/Ph. Zone 1A, marine/carbonate; 1B, marine and lacustrine (sulfate-rich); 1C, lacustrine/mixed (mature mudstone); 1D, lacustrine/mixed (high-rank coal); 2, lacustrine (sulfate-poor); 3, marine and other lacustrine; 4, shallow lake/deltaic/fluvial. Data points are from Table S3; zone classification follows [52].

The sterane/hopane ratio (S/H) reflects the predominance of eukaryotic over prokaryotic production [5]; high values indicate eutrophication and elevated photic-zone productivity. S/H increases with C_{27}-sterane abundance and decreases with C_{29}-sterane abundance (Figure 12c), so high S/H reflects phytoplankton rather than C_{29}-producing organisms. Moderate S/H combined with high C_{27} steranes in the Huangshanjie Formation implies contributions from both prokaryotes and terrigenous OM; the low S/H of the Taliqike and Kezilenuer formations (means 0.08 and 0.12) reflects the dominance of terrigenous OM; and the highest S/H, in the Qiakemake Formation, reflects a phytoplankton-dominated community [45]. Finally, the ADBT/ADBF ratio discriminates environmental type because dibenzothiophenes are end products of reactions between reduced sulfur and OM during deposition and diagenesis, whereas dibenzofurans derive from higher plants and lichens and therefore track terrestrial input [52]. Both Qiakemake samples and three of the five Huangshanjie samples plot in Zone 3 (lacustrine) and the other two Huangshanjie samples in Zones 2 and 4; the Yangxia samples are divided between Zones 3 and 4, with one sample (KPL4) in Zone 1B; the two Taliqike samples plot in Zones 2 (KPL2) and 4 (KLS3); and both Kezilenuer samples plot in Zone 4, the shallow-lake, deltaic, and fluvial field (Figure 12d). The ADBT/ADBF classification therefore places the Qiakemake and Huangshanjie samples on the aquatic side and the Kezilenuer samples on the terrigenous side, with the Yangxia and Taliqike formations transitional, in the same order as the maceral and terpane records. Taken with Section 5.3, the environmental and biological records therefore vary together and in the sense H2 predicts.

5.5. A Coupled Model of Paleoenvironmental and Organic-Matter Evolution

The parameters discussed above define, horizon by horizon, a coupled succession in which depositional environment and OM source co-evolve (Figure 13; Table 4). Stratigraphic and subsidence analyses show that the belt remained a continental lacustrine basin throughout the Mesozoic, but that the basin type switched from foreland to extensional rift at the Triassic–Jurassic angular unconformity (Figure 2); that switch reorganized accommodation and subsidence and, acting together with the CIA-recorded warm, humid climate, controlled lake hydrology. Because SiO_2/Al_2O_3 and Ti/Al remained nearly constant (Section 5.2), it is that reorganization, and not a shift in detrital supply, that the horizon-to-horizon geochemical contrasts express, as H1 requires.

Table 4. Coupled synthesis of basin phase, paleoenvironment, organic-matter source, and the dominant control on source-rock quality for the five Triassic–Jurassic horizons of the northern tectonic belt. Rift, Jurassic–Paleogene extensional-rift phase; OM, organic matter; TOC, total organic carbon; HI, hydrogen index; CIA, chemical index of alteration.

Formation	Basin Phase	Depositional Setting	Climate (CIA)	Salinity and Redox	Dominant OM Source	Dominant Control on Source-Rock Quality
Qiakemake	Rift	Contracted shore–shallow and semi-deep lake	Drier (80.1)	Brackish; dysoxic	Phytoplankton and bacteria; minor terrigenous	Productivity and preservation with low dilution; highest HI
Kezilenuer	Rift	Braided-delta front and shore–shallow lake; highstand	Drying (79.5)	Fresh; oxic	Higher plants and freshwater microalgae	Dilution and oxidation; high TOC, low HI; strongly gas-prone

Table 4. *Cont.*

Formation	Basin Phase	Depositional Setting	Climate (CIA)	Salinity and Redox	Dominant OM Source	Dominant Control on Source-Rock Quality
Yangxia	Rift	Braided-delta plain and bays; mid-transgression	Warm, humid (81.4)	Brackish to fresh; suboxic to oxic	Higher plants plus algae	Rapid burial of coarse terrigenous particles offsets oxygenation
Taliqike	Foreland	Lakeshore swamp	Hottest, most humid (85.5)	Fresh; suboxic	Mixed terrigenous and aquatic; minor chlorophyll-c phytoplankton	High terrigenous flux with rapid burial; highest TOC, humic OM
Huangshanjie	Foreland	Expanding semi-deep to deep lake	Warm, humid (83.0)	Brackish to fresh, stratified; suboxic	Aquatic organisms; prokaryotes	Best preservation, but inflow disperses OM; lowest TOC

Huangshanjie stage (Figure 13a). Subdued tectonism and lake expansion under high water influx, indicated by elevated Ca/Al, formed semi-deep to deep lakes. The highest Sr and Sr/Ba of the succession (means 126 ppm and 0.31) indicate brackish water, consistent with a stratified, brackish–fresh column, and relatively high V/(V + Ni) and V/Cr with a median Pr/Ph of 1.4 indicate suboxic bottom waters that favored OM preservation. High sapropelinite, a high C_{27}/C_{29} ratio (second only to the Qiakemake Formation), and moderate S/H together imply a major aquatic contribution, although the relatively high tricyclic-terpane ratios show that terrigenous input was also substantial. Enhanced nutrient input during lake-level rise promoted aquatic accumulation and limited higher-plant input; abundant inflow supplied dissolved inorganic carbon and nitrate and sustained moderate to high productivity, with prokaryotes acting as important primary producers. The apparent paradox of this stage is that the same inflow that fertilized the lake also dispersed the OM, which is why TOC is the lowest of the five units (0.79–4.5 wt %) despite the most favorable preservation conditions.

Taliqike stage (Figure 13b). Deposition occurred in a lakeshore swamp under the hottest, most humid climate of the succession, recorded by the highest CIA (85.5), which drove terrigenous freshwater inflow carrying mixed OM [15]. This is reflected by high combined vitrinite and inertinite contents and by the ADBT/ADBF ratios. Low Sr/Ba (mean 0.18) and the highest V/(V + Ni) and Ni/Co of the succession indicate a freshwater, suboxic column with reduced salinity stratification. A marginally higher C_{28}-sterane abundance (mean 20.5%, $n = 2$) may indicate a minor contribution from chlorophyll-c-bearing phytoplankton, but the lowest S/H and $C_{23}TT/C_{30}H$ values (means 0.08 and 0.04) show that algal OM was subordinate to terrigenous OM, consistent with coal-measure deposition under a high terrigenous nutrient supply. This stage yields the highest TOC of the succession (up to 29.1 wt %) but low HI because the abundant OM is dominantly humic.

Yangxia stage (Figure 13c). Above the regional unconformity, a braided-delta plain and bay system with small braided channels developed during mid-transgression. Combined redox and salinity proxies indicate a suboxic–oxic, brackish–fresh column, and the wide scatter of Ca/Al within this unit records a repeatedly renewed and hydrologically unstable water body. High $C_{19}/C_{23}TT$ and $C_{20}/C_{23}TT$ and the highest $C_{24}TeT/C_{26}TT$ of the succession indicate a major terrigenous contribution, and the regular-sterane ternary

plot (Figure 11) confirms combined higher-plant and algal input. Because particle texture, size, and density control the time OM spends exposed to oxygen and other degrading agents [12], the larger terrigenous particles sank rapidly and partly offset the otherwise unfavorable, partly oxygenated conditions; preservation here was a sedimentological rather than a chemical achievement.

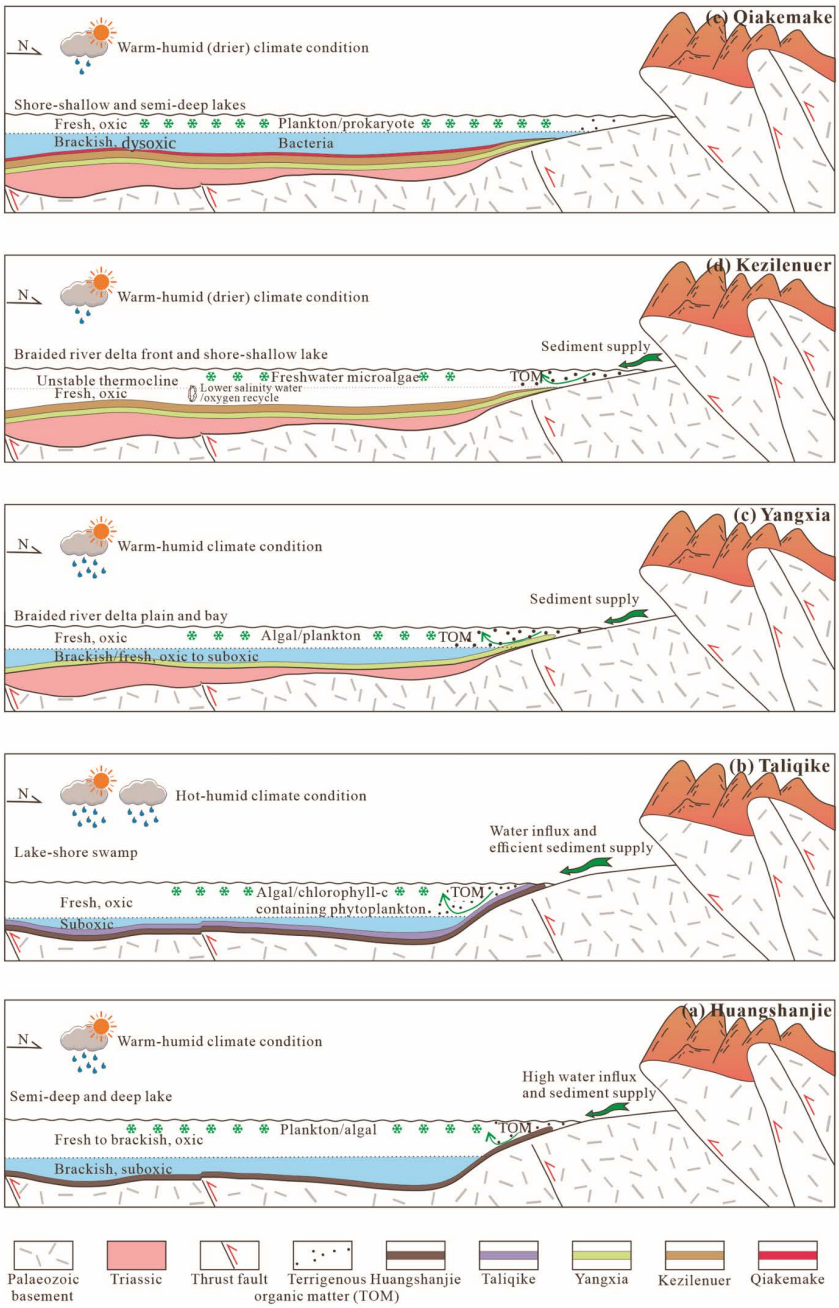


Figure 13. Coupled depositional and organic-matter models for the five source-rock horizons of the northern tectonic belt. (**a**) Suboxic, brackish–fresh, high-inflow semi-deep to deep lake with aquatic organisms (Huangshanjie stage); (**b**) freshwater lakeshore swamp with mixed terrigenous and aquatic OM (Taliqike stage); (**c**) suboxic–oxic braided-delta plain and bay with higher-plant plus algal OM (Yangxia stage); (**d**) oxic freshwater braided-delta front with dominant terrigenous OM and an unstable thermocline (Kezilenuer stage); (**e**) brackish, dysoxic semi-deep lake with dominant phytoplankton and bacteria (Qiakemake stage). TOM, terrigenous organic matter (referred to as terrigenous OM in the text).

Kezilenuer stage (Figure 13d). The climate became progressively drier, as recorded by the declining CIA (79.5). Deposition occurred on a braided-delta front and in a shore–shallow lake within the highstand systems tract during late transgression. The system was hydrologically open, with an unstable thermocline and freshwater salinity indicated by Sr and Sr/Ba. Very high Pr/Ph (average 5.03) and Pr/nC$_{17}$ (average 1.71), together with the highest inertinite content of the succession (mean 22%), indicate oxic conditions that nevertheless permitted coal-measure deposition with high TOC and type II$_2$–III kerogens. High terrigenous maceral contents and the ADBT/ADBF and Pr/Ph ratios indicate predominantly higher-plant OM, while the highest C$_{29}$-sterane abundance and a very low C$_{23}$TT/C$_{30}$H indicate terrigenous OM together with freshwater microalgae. Algal OM was preferentially degraded under oxic conditions, consistent with a low S/H; preferential algal degradation combined with terrigenous dilution left higher-plant input dominant [12]. The amorphous lamalginite and mineral–bituminous groundmass observed petrographically (Figure 3d) record exactly this history: initially algal material that was biodegraded and then mixed with clay to form organic–inorganic complexes.

Qiakemake stage (Figure 13e). By the late Middle Jurassic, the lake had contracted to the shore–shallow and semi-deep water body described in Section 2.2, from which meandering rivers and deltas were absent. Salinity rose to brackish levels, and a dysoxic column developed. The highest S/H, the lowest C$_{19}$/C$_{23}$TT, C$_{20}$/C$_{23}$TT, and C$_{24}$TeT/C$_{26}$TT, and the highest C$_{27}$-sterane abundance indicate major phytoplankton and minor terrigenous input. A substantial prokaryotic contribution may have driven eutrophication, increasing aquatic OM and shifting the OM type, as recorded by the *n*-alkane distribution and the CPI. Productivity was dominated by phytoplankton and bacterial biomass within a restricted brackish column with limited terrigenous supply, the configuration that yields the highest HI (up to 775 mg HC/g TOC) and the only liquid-prone interval in the column.

5.6. Relative Roles of Productivity, Preservation, and Dilution

Beyond its control on lake hydrology, basin type modulated clastic dilution directly. The Kuqa Depression was a foreland basin from the Late Permian through the Triassic and an extensional-rift basin from the Jurassic to the Paleogene. The Triassic sedimentation rate (approximately 60 m/Myr) exceeded the Jurassic rate (approximately 30 m/Myr), peaking in the Taliqike Formation and reaching a minimum in the Qiakemake Formation [39]. Because these averages derive from present-day thicknesses, the effects of decompaction, erosion at the Triassic–Jurassic unconformity, and the associated hiatus were evaluated (Table 5). Decompaction with the shale porosity–depth relation $\varphi = 0.63e^{-0.51z}$ (z in km) [67], for maximum burial depths of ~3.5–5 km (Triassic) and ~2.5–4 km (Jurassic), consistent with the R_o data, increases the present thicknesses by factors of 2.4–2.6 and 2.2–2.5, respectively, so that the Triassic/Jurassic rate ratio remains close to 2 (1.9–2.3). Erosion and the hiatus, applied to the Triassic interval only, can only raise its rate (by a factor of 1.2–1.7 for 10–30% erosion combined with a hiatus of 5–15% of the interval). The ordering foreland > rift is therefore robust, and it is this ordering, rather than the absolute values, that carries the argument. Rates below about 50 m/Myr generally favor OM preservation, whereas higher rates promote dilution [13]; as this threshold is empirical and the present rates are compacted minimum estimates, it is used only qualitatively: the foreland-to-rift transition moved the system from the dilution-dominated toward the preservation-dominated side of it. Critically, however, the wide TOC range observed (0.79–29.1 wt %) is inconsistent with the comparatively narrow spread of sedimentation rates, so rate alone cannot explain OM accumulation. What the high Triassic rates delivered was not merely rapid burial but a large terrigenous OM flux, and it is that flux thatfostered the high-TOC coal-measure source rocks of the Taliqike and, later, the Kezilenuer formations.

Table 5. Sensitivity of the Triassic/Jurassic sedimentation-rate contrast to decompaction, to erosion at the Triassic–Jurassic angular unconformity, and to the associated hiatus. Baseline rates are the present-thickness averages of [39]. Decompaction uses the shale porosity–depth function $\varphi = 0.63e^{-0.51z}$ (z in km) [67] with maximum burial depths bracketed from the R_o data; erosion is expressed as the fraction of the original Triassic thickness removed and the hiatus as the fraction of the nominal Triassic interval that it occupies (both applied to the Triassic phase only). The Triassic/Jurassic ratio remains ≥1.9 in every case.

Scenario	Triassic Foreland Phase (m/Myr)	Jurassic Rift Phase (m/Myr)	Triassic/Jurassic Ratio
Baseline: present-day thickness [39]	~60	~30	2.0
Decompacted; maximum burial 3.5 km (Triassic)/2.5 km (Jurassic)	~145	~67	2.2
Decompacted; maximum burial 4.5 km/3.5 km	~150	~73	2.1
Decompacted; maximum burial 5.0 km/4.0 km	~155	~74	2.1
Erosion of 10% of the Triassic section; hiatus = 5% of the interval	~70	~30	2.3
Erosion of 20%; hiatus = 10%	~83	~30	2.8
Erosion of 30%; hiatus = 15%	~100	~30	3.4

Synthesizing these observations yields the central result of this study and the test of H3. Basin-type switching from foreland to rift, together with the CIA-recorded climate, governed subsidence, lake hydrology, and hydrochemistry, which in turn set the biotic community and primary productivity; source-rock quality was then determined by the interplay among productivity, preservation, and dilution [1,10,13]. During Huangshanjie and Qiakemake deposition, the lake favored plankton and algal blooms and hence high bioproductivity; a large lake area limited terrigenous input, and brackish, suboxic bottom waters aided preservation, although during the Huangshanjie stage the high inflow that supplied the nutrients also dispersed the OM and lowered its abundance. During Taliqike, Yangxia, and Kezilenuer deposition, abundant terrigenous OM was delivered during transgression and subsequent lake-level fall, and the dominance of vitrinite marks the gas-prone character of these rocks. The suboxic–oxic, brackish–fresh Yangxia conditions and the suboxic Taliqike conditions were more favorable for preservation than the oxic Kezilenuer conditions. Differential sinking of larger terrigenous particles relative to smaller aquatic organisms controlled oxygen-exposure time, with larger particles shielding OM from degradation, while biological reworking enhanced oxidative degradation.

The deeper point is that these three terms are not independent. The same environments that govern OM production also govern its degradation and preservation; organisms both supply and consume OM; and sedimentation both preserves and dilutes it. Each horizon therefore represents a different resolution of the same three-way trade-off, and no single parameter (not TOC, not sedimentation rate, not redox state) ranks the horizons correctly on its own. H3 is accordingly supported, and this is why the column contains five vertically stacked, chemically distinct source-rock intervals, and why the mechanism rather than any individual control is what organizes the heterogeneity.

5.7. Implications for Source-Rock Prediction in Lacustrine Superimposed Basins

Because the model is mechanistic rather than descriptive, it can be inverted into a prediction procedure. Four operational implications follow.

First, TOC alone is a misleading ranking criterion in superimposed basins. In this succession, the TOC maximum (Taliqike, 29.1 wt %) and the HI maximum (Qiakemake, 775 mg HC/g TOC) occur in different units and record opposite environmental configurations: high terrigenous flux with rapid burial versus low clastic supply with high aquatic productivity. Screening intervals by TOC would select the gas-prone coal measures and

reject the only liquid-prone interval in the column. Paired TOC–HI screening, keyed to the environmental configuration, is therefore essential.

Second, the basin-phase boundary should be located before the geochemistry is interpreted because it sets the accommodation and dilution baseline against which every other signal is read. In the Kuqa Depression, that boundary is directly mappable as the Triassic–Jurassic regional angular unconformity, and crossing it halved the sedimentation rate, a contrast that survives decompaction and erosion corrections (Table 5), and moved the system from the dilution-dominated toward the preservation-dominated side of the approximately 50 m/Myr boundary that separates the two regimes [13]. In any superimposed basin, the equivalent surface predicts where a step change in source-rock character should be sought.

Third, the CIA provides an independent climatic axis that can be measured on cuttings and core alike and that is not available from organic data. Its use here converts a qualitative climate narrative into a quantitative control variable: the CIA maximum coincides with fresh water and with peak coal-measure development, and the decline of CIA into the Middle Jurassic ends in a restricted, brackish lake dominated by aquatic productivity. Where a CIA profile is read together with Sr/Ba, salinity, OM source, and, hence, probable kerogen, type can be anticipated before any biomarker analysis is undertaken.

Fourth, the workflow implied by this study is sequential and can be applied economically: (i) establish provenance stability from Al_2O_3–TiO_2, Ti/Al, and SiO_2/Al_2O_3, without which no environmental interpretation of the inorganic data is admissible; (ii) construct the CIA profile to obtain the climatic and hydrological framework; (iii) apply Sr/Ba and the trace-element redox proxies to define salinity and preservation potential; (iv) use macerals and terpane–sterane ratios to identify the OM source; and (v) combine these with the sedimentation-rate history to predict quality. Steps (i)–(iii) rely on inexpensive inorganic analyses and can be applied densely, with the more costly biomarker work reserved for calibration intervals.

The transferability of this framework is supported by the comparable behavior of other lacustrine systems in which input, preservation, and dilution have been evaluated jointly: the Dehui Depression of the Songliao Basin, where the same three-way interplay controls shale OM enrichment in a rift setting [13]; the Termit Basin, where depositional models were built from combined organic–geochemical and sequence–stratigraphic constraints [15,52]; and the Paleogene of the Bohai Bay Basin, where palynological and geochemical evidence together identified the controls on OM enrichment [1]. The Kuqa succession extends these cases to a column in which basin type itself changes so that a model tuned to one interval will mis-rank the others.

The same decoupling of TOC and source quality is recognized in rifted and deltaic coal-bearing basins elsewhere. The Tertiary Akata–Agbada source rocks of the Niger Delta are dominated by terrigenous, mainly type III OM; yet, they have generated large volumes of waxy oil as well as gas [68]; in the Bengal Basin, gas and condensates derive from terrestrial, higher-plant OM [69], and the Permian Gondwana coals of the half-graben fills are humic and predominantly gas-prone [70]; and in the Taranaki Basin, the poor correspondence between TOC, HI, and oil potential of coaly source rocks led to the recommendation that HI be read together with maceral composition [61]. In all of these basins, the TOC maximum need not coincide with the most oil-prone interval. What the Kuqa succession adds is that the weighting among OM supply, preservation, and dilution is reset when basin type changes within a single column, so that the foreland and rift phases require separate calibrations.

5.8. Limitations and Uncertainties

Several limitations qualify these conclusions and indicate where further work would be most valuable. The samples are outcrop material, and although the screening in Section 5.1.2 found no systematic weathering signature, it identified only one probably oxidized sample (KPL2, whose molecular redox ratios are therefore not used) and showed agreement with published well data for the same units; the comparison with subsurface material is indirect and some surface alteration of individual samples cannot be excluded; the absolute values of the most weathering-sensitive parameters (S_1, HI, and Th/U) from individual samples should therefore be treated as indicative rather than definitive. For the same reason, the emphasis throughout has been on relative differences between horizons, which are robust to a uniform weathering overprint, rather than on absolute thresholds.

Thermal maturity is a second constraint. With R_o up to 1.64% and T_{max} generally above 425 °C, some biomarker ratios, sterane and hopane distributions in particular, are partly maturity-dependent; although Section 5.1.4 shows that the between-horizon differences are not correlated with R_o, that test rests on 18 extracted samples, and aerobic reworking of biomass can further modify steroid and hopanoid parameters before burial in ways that are not maturity-related [45]. CPI and OEP close to unity confirm maturity and therefore limit the confidence with which small differences in these indices can be attributed to source alone. In addition, HI is suppressed in organic-lean mudstones by the mineral matrix and in coaly lithologies by the organic matrix (Section 5.1.3), and Rock-Eval parameters have recognized limitations in such samples [41]; the low HI of the Taliqike and Kezilenuer formations should therefore be read as evidence of humic OM rather than as a precise measure of generative potential.

Third, the proxy calibrations carry uncertainty. Most trace-element redox thresholds were established for marine systems, and their transfer to lacustrine settings is semi-quantitative; several published ranges overlap, which is why concordance between independent proxies rather than any single value was required here [48,49]; in addition, Th/U and V/Cr are partly controlled by dilution of the detrital fraction (Section 5.3). Sr/Ba is sensitive to barite precipitation, clay adsorption, and carbonate-hosted Sr as well as to salinity [50,51], and its weak correlation with CaO across the dataset ($r = 0.50$) means that the brackish signal of the CaO-richest Huangshanjie Formation may be slightly overstated. The CIA of organic-rich samples can be affected by dilution of the aluminosilicate fraction and by diagenetic carbonate; the A–CN–K trend (Figure 7b) and the sensitivity test (Table S4) show that neither potassium metasomatism nor the carbonate correction alters the Taliqike maximum or the Taliqike–Kezilenuer contrast, but XRD mineralogy, not available for these samples, would allow the correction to be made phase-specifically. Sedimentation rates are basin-scale averages; their foreland > rift ordering is robust to decompaction and erosion (Table 5), but the decompaction in Section 5.6 is a single-step correction based on an assumed burial history rather than a full backstripping model, and the rates do not capture local variability.

Finally, the analytical coverage is uneven: 46 samples were analyzed for bulk parameters and organic petrology, 32 for major and trace elements, and 18 by GC–MS, so the inorganic and molecular datasets provide fewer constraints per horizon than the bulk data; the molecular data for the Qiakemake, Kezilenuer, and Taliqike formations rest on two samples each, those for the Kezilenuer Formation from a single section; and formation-average CIA values are best resolved for the Taliqike, Kezilenuer, and Qiakemake formations. The outcrop sections lie along the piedmont and may not fully represent depocenter facies at equivalent stratigraphic levels. Targeted subsurface sampling, XRD mineralogy to make the CaO* correction phase-specific, higher-resolution CIA profiling through the Yangxia and Huangshanjie formations, and compound-specific isotope analysis would each strengthen

the model and are recommended as next steps. The model also makes a testable prediction: if basin-type switching rather than local facies variation is what reweights the three controls, depocenter sections should reproduce the same step change in the CIA–salinity–OM-source coupling across the Triassic–Jurassic unconformity that the piedmont sections show, displaced in absolute TOC but not in relative ordering. Failure to reproduce that step would favor a local-facies explanation instead.

6. Conclusions

(1) An integrated organic–inorganic dataset resolves strong vertical heterogeneity across the five Triassic–Jurassic source-rock units of the northern Kuqa Depression: TOC ranges from 0.79 to 29.1 wt %, HI from 19 to 775 mg HC/g TOC, and Pr/Ph from 0.61 to 8.8. The rocks are thermally mature and contain mainly type III (gas-prone) and type II–III (mixed) kerogens dominated by vitrinite and inertinite, with the Qiakemake Formation the only liquid-prone interval. Adding trace-element and CIA data, not previously available for the full column, was essential to interpreting this heterogeneity, and explicit screening showed that neither outcrop weathering, nor Rock-Eval matrix effects, nor thermal maturity controls the contrasts between horizons.

(2) Stable Al_2O_3–TiO_2 ($r^2 = 0.66$), Ti/Al and SiO_2/Al_2O_3 relationships show that the contrasts between horizons record environmental change rather than a change in provenance. Under the combined forcing of CIA-recorded paleoclimate and basin-type switching at the Triassic–Jurassic angular unconformity, the lake passed from Triassic brackish–fresh, stratified water bodies to freshwater swamps, then to oxic deltaic systems and finally, in the Middle Jurassic, to a dysoxic, brackish semi-deep water body. OM sources co-evolved from aquatic organisms, through mixed terrigenous–aquatic and higher-plant plus algal inputs, to terrigenous dominance, and finally phytoplankton.

(3) Quality was set by how primary productivity, preservation, and clastic dilution were balanced, and that balance shifted from horizon to horizon: high bioproductivity with brackish–suboxic preservation favored the Huangshanjie and Qiakemake source rocks, whereas a high terrigenous flux with rapid burial sustained the coal-measure source rocks of the Taliqike and Kezilenuer formations. Because the same environments that produce OM also degrade it, and because sedimentation both preserves and dilutes it, no single parameter ranks the horizons correctly, and the wide TOC range cannot be explained by the comparatively narrow spread of sedimentation rates, whose foreland > rift ordering is robust to decompaction and to erosion at the Triassic–Jurassic unconformity.

(4) The coupled model accounts for the vertical stacking of chemically distinct intervals within one column and can be inverted into a practical prediction procedure: locate the basin-phase boundary, establish provenance stability, construct a CIA profile, then apply salinity, redox, and OM-source proxies before ranking intervals on paired TOC–HI criteria rather than on TOC alone. Because the weighting among the three controls is reset at the phase boundary, a model calibrated on one interval should not be carried across it; in that sense, the framework is transferable to other lacustrine superimposed basins.

Supplementary Materials: The following supporting information can be downloaded at: https://www.mdpi.com/article/10.3390/pr14213467/s1. Table S1: bulk organic–geochemical parameters, maceral compositions, and vitrinite reflectance of the 46 samples; Table S2: major- and trace-element compositions and derived ratios (CIA, Sr/Ba, V/(V + Ni), Th/U, Ni/Co, V/Cr, Ca/Al, Ti/Al) of the 32 samples; Table S3: molecular biomarker and C_{29} sterane maturity parameters of the 18 extracted

samples; Table S4: sensitivity of the CIA to the CaO* correction; Table S5: screening of the outcrop dataset for weathering and Rock-Eval matrix effects; Table S6: thermal-maturity parameters of the extracted samples by formation; Table S7: correlation of the environmental biomarker ratios with R_o and T_{max}.

Author Contributions: Conceptualization, W.L. and X.L.; methodology, W.L. and Q.W.; validation, X.L. and Q.W.; formal analysis, W.L. and X.L.; investigation, W.L., J.L. and M.L.; resources, J.L., M.L. and Z.X.; data curation, W.L. and G.Z.; writing—original draft preparation, W.L.; writing—review and editing, X.L.; visualization, W.L. and Q.W.; supervision, X.L.; project administration, X.L.; funding acquisition, X.L. and W.L. All authors have read and agreed to the published version of the manuscript.

Funding: This research was funded by the National Science and Technology Major Project of China (Nos. 2016ZX05007-003 and 2025ZD1408802-02), Postdoctoral Research Program of Sinopec Jianghan Oilfield Company (JHYTZL2025112802), the Science and Technology Projects of PetroChina (No. T11083), the National Natural Science Foundation of China (Nos. U1810201, U22B6002), and the Fundamental Research Funds for the Central Universities (Nos. 2020YJSMT02, 2022YJSMT03).

Data Availability Statement: The original contributions presented in this study are included in the article/Supplementary Materials. Further inquiries can be directed to the corresponding author.

Acknowledgments: The authors thank Li Liu and Qian Zhang for their support during this study, and the reviewers and editors for their constructive comments.

Conflicts of Interest: W.L. is employed by the company Sinopec Jianghan Oilfield Company; J.L. and M.L. are employed by the company PetroChina Research Institute of Petroleum Exploration & Development; Z.X. is employed by the company Tarim Oilfield Company, PetroChina. The remaining authors declare that the research was conducted in the absence of any commercial or financial relationships that could be construed as a potential conflict of interest. The funders and the above companies had no role in the design of the study; in the collection, analyses, or interpretation of data; in the writing of the manuscript; or in the decision to publish the results.

Abbreviations

The following abbreviations are used in this manuscript:

ADBF	Alkyldibenzofuran
ADBT	Alkyldibenzothiophene
CIA	Chemical index of alteration
CPI	Carbon preference index
EOM	Extractable organic matter
GC–MS	Gas chromatography–mass spectrometry
HI	Hydrogen index
ICP-MS	Inductively coupled plasma mass spectrometry
OEP	Odd–even predominance
OM	Organic matter
Ph	Phytane
Pr	Pristane
R_o	Vitrinite reflectance
S/H	Sterane/hopane ratio
TeT	Tetracyclic terpane
TOC	Total organic carbon
TOM	Terrigenous organic matter (Figure 13)
TT	Tricyclic terpane
XRF	X-ray fluorescence

References

1. Zhao, Z.; Hou, D.; Cheng, X.; Xu, H.; Ma, C.; Zhou, X.; Xu, C. Geochemical and Palynological Characteristics of the Paleogene Source Rocks in the Northeastern Laizhouwan Sag, Bohai Bay Basin, China: Hydrocarbon Potential, Depositional Environment, and Factors Controlling Organic Matter Enrichment. *Mar. Pet. Geol.* **2021**, *124*, 104792. [CrossRef]
2. Zhao, G.; Li, X.; Liu, M.; Li, J.; Liu, Y.; Zhang, X.; Wei, Q.; Xiao, Z. Accumulation Characteristics and Controlling Factors of the Tugeerming Gas Reservoir in the Eastern Kuqa Depression of the Tarim Basin, Northwest China. *J. Pet. Sci. Eng.* **2022**, *217*, 110881. [CrossRef]
3. Dai, J.; Gong, D.; Ni, Y.; Huang, S.; Wu, W. Stable Carbon Isotopes of Coal-Derived Gases Sourced from the Mesozoic Coal Measures in China. *Org. Geochem.* **2014**, *74*, 123–142. [CrossRef]
4. Gao, T.Z.; Ding, X.J.; Yang, X.Z.; Chen, C.C.; Xu, Z.P.; Liu, K.Y.; Zhang, X.Q.; Cao, W.Z. Geochemical Characteristics and Depositional Environment of Coal-Measure Hydrocarbon Source Rocks in the Northern Tectonic Belt, Kuqa Depression. *Appl. Sci.* **2022**, *12*, 9464. [CrossRef]
5. Guo, X.S.; Wang, E.Z.; Ma, X.X.; Li, M.W.; Qian, M.H.; Cao, T.T.; Li, Z.M.; Chu, J.J. Lacustrine Shale Oil Systems in China: Advances in Characterization Methods and Resource Accumulation Models. *Earth Sci. Rev.* **2025**, *270*, 105256. [CrossRef]
6. Hu, S.Y.; Bai, B.; Tao, S.Z.; Bian, C.S.; Zhang, T.S.; Chen, Y.Y.; Liang, X.W.; Wang, L.; Zhu, R.K.; Jia, J.H.; et al. Heterogeneous Geological Conditions and Differential Enrichment of Medium and High Maturity Continental Shale Oil in China. *Pet. Explor. Dev.* **2022**, *49*, 257–271. [CrossRef]
7. Ding, X.J.; Gao, T.Z.; Yang, X.Z.; Xu, Z.P.; Chen, C.C.; Liu, K.Y.; Zhang, X.Q. Jurassic Paleoclimate Reconstruction and Its Influence on Organic Matter Enrichment in Kuqa Depression, Tarim Basin. *J. Geol.* **2023**, *131*, 97–115. [CrossRef] [PubMed]
8. Zhao, N.; Ye, J.; Yang, B.; Zhang, F.; Yu, H.; Xu, C.; Xu, S.; Xu, J.; Shu, Y. Depositional Palaeoenvironment and Models of the Eocene Lacustrine Source Rocks in the Northern South China Sea. *Mar. Pet. Geol.* **2021**, *128*, 105015. [CrossRef]
9. Zhang, S.C.; Wang, X.M.; Zhang, B. Breakthrough and Perspective in the Theory of Hydrocarbon Generation for Alkaline Lake Source Rocks. *Sci. China Earth Sci.* **2025**, *68*, 725–740. [CrossRef]
10. Qi, K.; Ren, Z.; Chen, Z.; Cui, J. Characteristics and Controlling Factors of Lacustrine Source Rocks in the Lower Cretaceous, Suhongtu Depression, Yin-E Basin, Northern China. *Mar. Pet. Geol.* **2021**, *127*, 104943. [CrossRef]
11. Xu, S.; Wang, Y.X.; Bai, N.; Wu, S.Q.; Liu, B.C. Organic Matter Enrichment Mechanism in Saline Lacustrine Basins: A Review. *Geol. J.* **2024**, *59*, 155–168. [CrossRef]
12. Benavente, C.A.; Bohacs, K.M. Advances in Limnogeology: The Lake-Basin-Type Model Revisited 25 Years After...anomalies, Conundrums and Upgrades. *Depos. Rec.* **2024**, *10*, 748–792. [CrossRef]
13. Xu, Z.J.; Wang, Y.; Jiang, S.; Fang, C.; Liu, L.F.; Wu, K.J.; Luo, Q.; Li, X.; Chen, Y.Y. Impact of Input, Preservation and Dilution on Organic Matter Enrichment in Lacustrine Rift Basin: A Case Study of Lacustrine Shale in Dehui Depression of Songliao Basin, NE China. *Mar. Pet. Geol.* **2022**, *135*, 105386. [CrossRef]
14. Sachsenhofer, R.F.; Popov, S.V.; Akhmetiev, M.A.; Bechtel, A.; Gratzer, R.; Gross, D.; Horsfield, B.; Rachetti, A.; Rupprecht, B.; Schaffar, W.B.H.; et al. The Type Section of the Maikop Group (Oligocene-Lower Miocene) at the Belaya River (North Caucasus): Depositional Environment and Hydrocarbon Potential. *AAPG Bull.* **2017**, *101*, 289–319. [CrossRef]
15. Lai, H.; Li, M.; Liu, J.; Mao, F.; Xiao, H.; He, W.; Yang, L. Organic Geochemical Characteristics and Depositional Models of Upper Cretaceous Marine Source Rocks in the Termit Basin, Niger. *Palaeogeogr. Palaeoclimatol. Palaeoecol.* **2018**, *495*, 292–308. [CrossRef]
16. Pla, O.; Roca, E.; Xie, H.; Izquierdo-Llavall, E.; Muñoz, J.A.; Rowan, M.G.; Ferrer, O.; Gratacós, Ò.; Yuan, N.; Huang, S. Influence of Syntectonic Sedimentation and Décollement Rheology on the Geometry and Evolution of Orogenic Wedges: Analog Modeling of the Kuqa Fold-and-Thrust Belt (NW China). *Tectonics* **2019**, *38*, 2727–2755. [CrossRef]
17. Horton, B.K.; Capaldi, T.N.; Mackaman-Lofland, C.; Perez, N.D.; Bush, M.A.; Fuentes, F.; Constenius, K.N. Broken Foreland Basins and the Influence of Subduction Dynamics, Tectonic Inheritance, and Mechanical Triggers. *Earth Sci. Rev.* **2022**, *234*, 104193. [CrossRef]
18. Horton, B.K. Sedimentary Record of Andean Mountain Building. *Earth Sci. Rev.* **2018**, *178*, 279–309. [CrossRef]
19. Pérez-Gussinyé, M.; Collier, J.S.; Armitage, J.J.; Hopper, J.R.; Sun, Z.; Ranero, C.R. Towards a Process-Based Understanding of Rifted Continental Margins. *Nat. Rev. Earth Environ.* **2023**, *4*, 166–184. [CrossRef]
20. Pang, X.; Peng, J.; Jiang, Z.; Yang, H.; Wang, P.; Jiang, F.; Wang, K. Hydrocarbon Accumulation Processes and Mechanisms in Lower Jurassic Tight Sandstone Reservoirs in the Kuqa Subbasin, Tarim Basin, Northwest China: A Case Study of the Dibei Tight Gas Field. *AAPG Bull.* **2019**, *103*, 769–796. [CrossRef]
21. Wang, Q.H.; Yang, H.J.; Yang, W.; Xu, Z.P. New Progress and Future Exploration Targets in Petroleum Geological Research of Ultra-Deep Clastic Rocks in Kuqa Depression, Tarim Basin, NW China. *Pet. Explor. Dev.* **2025**, *52*, 79–94. [CrossRef]
22. Zhao, W.Z.; Zhang, S.C.; Wang, F.Y.; Cramer, B.; Chen, J.P.; Sun, Y.G.; Zhang, B.M.; Zhao, M.J. Gas Systems in the Kuche Depression of the Tarim Basin: Source Rock Distributions, Generation Kinetics and Gas Accumulation History. *Org. Geochem.* **2005**, *36*, 1583–1601. [CrossRef]

23. Huang, W.K.; Zeng, L.F.; Pan, C.C.; Xiao, Z.Y.A.; Zhang, H.Z.; Huang, Z.B.; Zhao, Q.; Yu, S.; Xu, H.; Chen, C.S.; et al. Petroleum Generation Potentials and Kinetics of Coaly Source Rocks in the Kuqa Depression of Tarim Basin, Northwest China. *Org. Geochem.* **2019**, *133*, 32–52. [CrossRef]
24. Yang, X.Z.; Dong, C.Y.; Zhang, L.; Xu, Z.P.; Li, J. Triassic-Jurassic Hydrocarbon Source Rock Comparison in the Northern Kuqa Depression, Tarim Basin: Geochemical Characteristics and Hydrocarbon Potential. *Appl. Geophys.* **2025**, *22*, 1–20. [CrossRef]
25. Fan, S.; Lu, Y.H.; Li, L.; Wei, H.; Zhang, H.F.; Shen, L. Geochemical Characteristics, Distribution and Petroleum Geological Significance of Triassic-Jurassic Source Rocks in the Tugeerming and Surrounding Areas of Kuqa Depression, Tarim Basin. *Nat. Gas Geosci.* **2022**, *33*, 2074–2086. [CrossRef]
26. Ding, X.J.; Gao, T.Z.; Yang, X.Z.; Xu, Z.P.; Chen, C.C.; Liu, K.Y.; Zhang, X.Q. Geochemical Characteristics and Development Model of the Coal-Measure Source Rock in the Kuqa Depression of Tarim Basin. *Processes* **2023**, *11*, 1777. [CrossRef]
27. Zhang, W.J.; Zhang, W.Y.; Lin, S.M.; Ke, X.; Xiang, W.; He, T.H.; Zhang, M. Characteristics and Genesis of Biomarker Assemblages of Mesozoic Coal Measure Source Rocks in the Kuqa Depression, Tarim Basin, China. *Processes* **2023**, *11*, 2885. [CrossRef]
28. Li, J.; Yang, X.Z.; Dong, C.Y.; Li, J.; Xu, Z.P.; Zhang, L.; Zhang, W. Characteristics of Orderly Hydrocarbon Accumulation of Deep Reservoirs in Kuqa Depression and Its Exploration Implications. *Geol. J.* **2023**, *58*, 4103–4120. [CrossRef]
29. Li, D.J.; Zhao, Q.; Zhao, L.Y.; Chen, Y.P.; Deng, Z.; Chang, X.C.; Shi, B.B.; Han, R.Y.; Wang, S.B. Differential Enrichment Mechanisms of Organic Matter in Middle-Upper Triassic Lacustrine Mudstone, North Kuqa Depression (Tarim Basin, China): An Integrated Approach Utilizing Inorganic and Organic Geochemical Evidence. *Acta Geochim.* **2026**, *45*, 422–438. [CrossRef]
30. Liang, W.; Li, X.; Wei, Q.; Li, J.; Sun, K.; He, Y.; Zhang, Y. Element geochemical characteristics of Mesozoic mudstones in the northern piedmont zone of the Kuqa depression and their implications to sedimentary environments. *J. Min. Sci. Technol.* **2019**, *4*, 375–383. (In Chinese with English abstract)
31. Niu, H.; Liang, L.; Wang, L.; Wang, C.; Zhang, J. Study on Sedimentation Distribution Based on Cooperative Analysis of Geologic–Geophysical in Less Well Area: A Case Study of Suweiyi Sandstone in the DB Area, Kuqa Depression in Tarim Basin. *Pet. Res.* **2020**, *5*, 339–346. [CrossRef]
32. Wei, Q.; Li, X.; Sun, K.; Liang, W.; Feng, S.; Zhang, G.; Xiao, Z. Hydrocarbon Geochemistry and Charging History of the Deep Tight Sandstone Reservoirs in the Dabei Gas Field, Kuqa Depression, Tarim Basin, NW China. *Energy Explor. Exploit.* **2020**, *38*, 2325–2355. [CrossRef]
33. Lai, J.; Li, D.; Bai, T.Y.; Zhao, F.; Ai, Y.; Liu, H.K.; Cai, D.Y.; Wang, G.W.; Chen, K.J.; Xie, Y.Q. Reservoir Quality Evaluation and Prediction in Ultra-Deep Tight Sandstones in the Kuqa Depression, China. *J. Struct. Geol.* **2023**, *170*, 104850. [CrossRef]
34. Zhao, G.; Li, X.; Liu, M.; Dong, C.; Chen, D.; Zhang, J. Reservoir Characteristics of Tight Sandstone and Sweet Spot Prediction of Dibei Gas Field in Eastern Kuqa Depression, Northwest China. *Energies* **2022**, *15*, 3135. [CrossRef]
35. Song, X.; Lu, X.X.; Quan, H.; Zhou, X.X.; Guan, Y.; Feng, X.L. Recovery of the Cretaceous Palaeo-Uplifts and Its Implications for Hydrocarbon Systems in the Kuqa Depression, Tarim Basin, Western China. *Geol. J.* **2020**, *55*, 7872–7891. [CrossRef]
36. Wei, L.; Huang, S.; Luo, C.; Duan, Y.; Xia, J.; Zhong, Z.; Li, X.; Chang, H. Reconstruction of the Proto-Type Basin and Tectono-Paleographical Evolution of Tarim in the Cenozoic. *Front. Earth Sci.* **2023**, *11*, 1095002. [CrossRef]
37. Jia, K.; Zeng, J.H.; Ma, Y.; Wang, Q.H.; Xu, Z.P. Hydrocarbon Generation and Accumulation in the Eastern Kuqa Depression, Northwestern China: Insights from Basin and Petroleum System Modeling. *Appl. Sci.* **2024**, *14*, 1217. [CrossRef]
38. Zhang, S.C.; Zhang, B.; Zhu, G.Y.; Wang, H.T.; Li, Z.X. Geochemical Evidence for Coal-Derived Hydrocarbons and Their Charge History in the Dabei Gas Field, Kuqa Thrust Belt, Tarim Basin, NW China. *Mar. Pet. Geol.* **2011**, *28*, 1364–1375. [CrossRef]
39. Li, Y.; Qi, J.; Shi, J.; Sun, T.; Xu, Z.; Yu, H.; Zhang, W.; Yang, X. Characteristics of Mesozoic Basin in Kuqa Depression, Tarim Basin. *Geotecton. Metallog.* **2017**, *41*, 829–842. [CrossRef]
40. Du, J.H.; Wang, Z.M.; Hu, S.Y.; Wang, Q.H.; Xie, H.W. Formation Conditions and Geological Characteristics of Deep Giant Gas Provinces in the Kuqa Foreland Thrust Belt. *Pet. Explor. Dev.* **2012**, *39*, 413–422. [CrossRef]
41. Zhang, S.; Wang, D.; Wang, Y. Remarkable Issues of Rock-Eval Pyrolysis in the Assessment of Shale Oil/Gas. *Oil Gas Geol.* **2023**, *44*, 1020–1032. [CrossRef]
42. *ISO 7404-2:2009*; Methods for the Petrographic Analysis of Coals — Part 2: Methods of Preparing Coal Samples. ISO: Geneva, Switzerland, 2009.
43. *ISO 7404-5:2009*; Methods for the Petrographic Analysis of Coals — Part 5: Method of Determining Microscopically the Reflectance of Vitrinite. ISO: Geneva, Switzerland, 2009.
44. *ASTM D7708-14*; Standard Test Method for Microscopical Determination of the Reflectance of Vitrinite Dispersed in Sedimentary Rocks. ASTM International: West Conshohocken, PA, USA, 2014.
45. Bobrovskiy, I.; Poulton, S.W.; Hope, J.M.; Brocks, J.J. Impact of Aerobic Reworking of Biomass on Steroid and Hopanoid Biomarker Parameters Recording Ecological Conditions and Thermal Maturity. *Geochim. Cosmochim. Acta* **2024**, *364*, 114–128. [CrossRef]
46. Nesbitt, H.W.; Young, G.M. Early Proterozoic Climates and Plate Motions Inferred from Major Element Chemistry of Lutites. *Nature* **1982**, *299*, 715–717. [CrossRef]
47. McLennan, S.M. Weathering and Global Denudation. *J. Geol.* **1993**, *101*, 295–303. [CrossRef]

48. Hoogakker, B.A.A.; Davis, C.; Wang, Y. Reviews and Syntheses: Review of Proxies for Low-Oxygen Paleoceanographic Reconstructions. *Biogeosciences* **2025**, *22*, 863–957. [CrossRef]
49. Algeo, T.J.; Li, C. Redox Classification and Calibration of Redox Thresholds in Sedimentary Systems. *Geochim. Cosmochim. Acta* **2020**, *287*, 8–26. [CrossRef]
50. Wei, W.; Algeo, T.J.; Lu, Y.; Lu, Y.; Liu, H.; Zhang, S.; Peng, L.; Zhang, J.; Chen, L. Identifying Marine Incursions into the Paleogene Bohai Bay Basin Lake System in Northeastern China. *Int. J. Coal Geol.* **2018**, *200*, 1–17. [CrossRef]
51. Wei, W.; Algeo, T.J. Elemental Proxies for Paleosalinity Analysis of Ancient Shales and Mudrocks. *Geochim. Cosmochim. Acta* **2020**, *287*, 341–366. [CrossRef]
52. Xiao, H.; Wang, T.G.; Li, M.; Lai, H.; Liu, J.; Mao, F.; Tang, Y. Geochemical Characteristics of Cretaceous Yogou Formation Source Rocks and Oil-Source Correlation within a Sequence Stratigraphic Framework in the Termit Basin, Niger. *J. Pet. Sci. Eng.* **2019**, *172*, 360–372. [CrossRef]
53. El Atfy, H.; Ghassal, B.I. *Advances in Petroleum Source Rock Characterizations: Integrated Methods and Case Studies*; Springer: Cham, Switzerland, 2023; ISBN 978-3-031-16395-1.
54. Li, Y.; Pan, S.Q.; Ning, S.Z.; Shao, L.Y.; Jing, Z.H.; Wang, Z.S. Coal Measure Metallogeny: Metallogenic System and Implication for Resource and Environment. *Sci. China Earth Sci.* **2022**, *65*, 1211–1228. [CrossRef]
55. Clayton, J.L.; Swetland, P.J. Subaerial Weathering of Sedimentary Organic Matter. *Geochim. Cosmochim. Acta* **1978**, *42*, 305–312. [CrossRef]
56. Littke, R.; Klussmann, U.; Krooss, B.; Leythaeuser, D. Quantification of Loss of Calcite, Pyrite, and Organic Matter Due to Weathering of Toarcian Black Shales and Effects on Kerogen and Bitumen Characteristics. *Geochim. Cosmochim. Acta* **1991**, *55*, 3369–3378. [CrossRef]
57. Petsch, S.T.; Berner, R.A.; Eglinton, T.I. A Field Study of the Chemical Weathering of Ancient Sedimentary Organic Matter. *Org. Geochem.* **2000**, *31*, 475–487. [CrossRef]
58. Tribovillard, N.; Algeo, T.J.; Lyons, T.; Riboulleau, A. Trace Metals as Paleoredox and Paleoproductivity Proxies: An Update. *Chem. Geol.* **2006**, *232*, 12–32. [CrossRef]
59. Espitalié, J.; Madec, M.; Tissot, B. Role of Mineral Matrix in Kerogen Pyrolysis: Influence on Petroleum Generation and Migration. *AAPG Bull.* **1980**, *64*, 59–66. [CrossRef]
60. Peters, K.E. Guidelines for Evaluating Petroleum Source Rock Using Programmed Pyrolysis. *AAPG Bull.* **1986**, *70*, 318–329. [CrossRef]
61. Sykes, R.; Snowdon, L.R. Guidelines for Assessing the Petroleum Potential of Coaly Source Rocks Using Rock-Eval Pyrolysis. *Org. Geochem.* **2002**, *33*, 1441–1455. [CrossRef]
62. Peters, K.E.; Walters, C.C.; Moldowan, J.M. *The Biomarker Guide, Volume 2: Biomarkers and Isotopes in Petroleum Exploration and Earth History*, 2nd ed.; Cambridge University Press: Cambridge, UK, 2005; ISBN 978-0-521-83762-0.
63. Fedo, C.M.; Nesbitt, H.W.; Young, G.M. Unraveling the Effects of Potassium Metasomatism in Sedimentary Rocks and Paleosols, with Implications for Paleoweathering Conditions and Provenance. *Geology* **1995**, *23*, 921–924. [CrossRef]
64. Xia, L.; Cao, J.; Hu, W.; Zhi, D.; Tang, Y.; Li, E.; He, W. Coupling of Paleoenvironment and Biogeochemistry of Deep-Time Alkaline Lakes: A Lipid Biomarker Perspective. *Earth Sci. Rev.* **2021**, *213*, 103499. [CrossRef]
65. Liu, B.; Mastalerz, M.; Schieber, J. SEM Petrography of Dispersed Organic Matter in Black Shales: A Review. *Earth Sci. Rev.* **2022**, *224*, 103874. [CrossRef]
66. Huang, W.-Y.; Meinschein, W.G. Sterols as Ecological Indicators. *Geochim. Cosmochim. Acta* **1979**, *43*, 739–745. [CrossRef]
67. Sclater, J.G.; Christie, P.A.F. Continental Stretching: An Explanation of the Post-Mid-Cretaceous Subsidence of the Central North Sea Basin. *J. Geophys. Res.* **1980**, *85*, 3711–3739. [CrossRef]
68. Tuttle, M.L.W.; Charpentier, R.R.; Brownfield, M.E. *The Niger Delta Petroleum System: Niger Delta Province, Nigeria, Cameroon, and Equatorial Guinea, Africa*; U.S. Geological Survey Open-File Report 99-50-H; U.S. Geological Survey: Reston, VA, USA, 1999.
69. Curiale, J.A.; Covington, G.H.; Shamsuddin, A.H.M.; Morelos, J.A.; Shamsuddin, A.K.M. Origin of Petroleum in Bangladesh. *AAPG Bull.* **2002**, *86*, 625–652. [CrossRef]
70. Farhaduzzaman, M.; Abdullah, W.H.; Islam, M.A. Depositional Environment and Hydrocarbon Source Potential of the Permian Gondwana Coals from the Barapukuria Basin, Northwest Bangladesh. *Int. J. Coal Geol.* **2012**, *90–91*, 162–179. [CrossRef]

Disclaimer/Publisher's Note: The statements, opinions and data contained in all publications are solely those of the individual author(s) and contributor(s) and not of MDPI and/or the editor(s). MDPI and/or the editor(s) disclaim responsibility for any injury to people or property resulting from any ideas, methods, instructions or products referred to in the content.